2014-03-01

U-Pu-Zr Alloy Design by Ternary Potts-Phase Field Modeling

Jordan Jeffrey Cox
Brigham Young University - Provo

U-Pu-Zr Alloy Design by Ternary Potts-Phase Field Modeling

Jordan J. Cox

A thesis submitted to the faculty of
Brigham Young University
in partial fulfillment of the requirements for the degree of

Master of Science

Eric R. Homer, Chair
David T. Fullwood
Tracy W. Nelson

Department of Mechanical Engineering

Brigham Young University

March 2014

ABSTRACT

U-Pu-Zr Alloy Design by Ternary Potts-Phase Field Modeling

Jordan J. Cox
Department of Mechanical Engineering, BYU
Master of Science

U-Pu-Zr nuclear fuels experience a redistribution of constituents and a number of phase transformations when subjected to the thermal gradient present in nuclear reactors. This redistribution and phase separation leads to several undesirable fuel performance issues. In an effort to better understand how different alloys compositions are affected by this thermal gradient, we utilize the recently introduced Hybrid Potts-phase Field Method to study the U-Pu-Zr system. The recently introduced Hybrid method couples microstructural and compositional evolutions of a system so that the two phenomena can be studied together rather than separately, as is frequently done. However, simulation of the U-Pu-Zr system required several adaptations to the modeling framework. First the model was adapted to incorporate a thermodynamic database for free energy calculations, as well as thermal diffusion (the Soret effect). These abilities were tested in the Al-Si system. Second, the modeling framework was expanded to simulate three component systems such that ternary U-Pu-Zr alloys could be studied.

Simulations capture constituent redistribution and the appropriate phase transformations as compared to experimentally irradiated a U-16Pu-23Zr (at%) nuclear fuel. Additional simulations analyze constituent redistribution over the entire spectrum of U-Pu-Zr compositions. Analysis of these simulation results indicate alloys that are likely to experience minimal constituent redistribution and fewer phase boundaries, such that their fuel performance should be improved. The outcomes of the work include a coupled microstructural-compositional modeling framework for ternary alloys and suggestions of U-Pu-Zr alloys that could lead to improved fuel performance.

Keywords: Potts-phase field, thermodynamic database, U-Pu-Zr

ACKNOWLEGMENTS

I would like to express my special appreciation and thanks to my advisor Professor Eric Homer, who has been a tremendous mentor for me. I would like to thank him for his encouraging words throughout my research and continued education. His advice on both research, as well as on my career, were very supportive and influential. I would also like to thank Professor David Fullwood and Professor Dr. Tracy Nelson for serving as my committee members, as well as their guidance throughout various courses.

I'd also like to give my thanks to Sandia National Laboratories for the funding for this research. Sandia National Laboratories is a multiprogram laboratory managed and operated by Sandia Corporation, a wholly owned subsidiary of Lockheed Martin Corporation, for the U.S. Department of Energy's National Security Administration under contract DE-AC04-94AL85000.

Lastly, a special thanks to my family. Words cannot express how grateful I am to my wife Lindsay for all of the sacrifices that she made on my behalf. Her support was what sustained me. I would also like to thank all of my friends, both in and away from the lab, who supported and assisted me.

TABLE OF CONTENTS

LIST OF TABLES

LIST OF FIGURES

1 INTRODUCTION

The thermal and mechanical properties of materials, and their alloys, are strongly dependent upon the microstructure and phase of the material, both of which are effected by the material's composition. Environmental influences, such as a thermal gradient, can cause the constituents of an alloy to migrate, thus altering the local composition. Compositional changes can, in turn, alter the phase, microstructure and, ultimately, the material properties. This material property alteration, due to a redistribution of constituents under a thermal gradient, is observed in the U-Pu-Zr metallic nuclear fuel alloys.

U-Pu-Zr is considered an advanced fast reactor fuel because of its superior properties for high burnup, thermal response and inherent safety (1). While limited characterization and performance data is available for the performance of systems of this particular alloy, it is clear that three concentric zones are formed when U-Pu-Zr is irradiated or subject to a thermal gradient (2) (3), as shown in Figure 1-1 (4). These zones are compositionally and microstructurally inhomogeneous. This inhomogeneity alters the fuel behavior and performance, in that it causes phase transformations, solidus temperature changes and changes in the fissile atom density. Computational methods are often used to model the evolution of such alloys, as a means to demonstrate and predict their behavior. Two of the primary material evolutions that are commonly modeled computationally are microstructural and compositional.

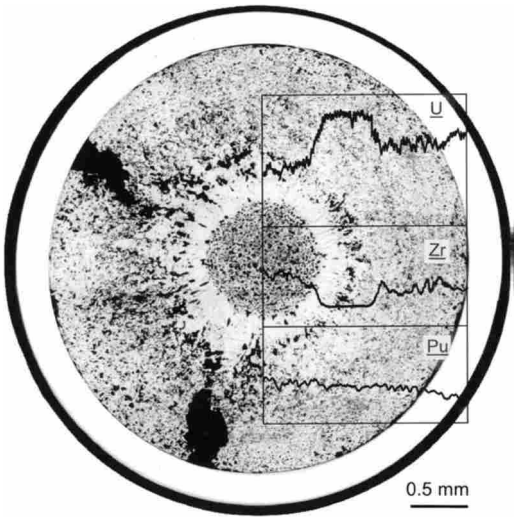

Figure 1-1 A Micrograph of Irradiated U-Pu-Zr Fuel. Radial composition profiles overlain, showing the three concentric zones: the Zr enriched center zone, Uranium enriched intermediate zone and relatively unchanged outer zone.

Microstructural and compositional evolutions represent two key phenomena influencing the processing and performance of alloyed materials. The local microstructure is usually described in terms of the grains and grain boundaries while the composition focuses on constituent and phase distribution. These two phenomena are fundamentally linked, but due to their respective complexities are frequently modeled individually (5). Recent work developed a new Hybrid Potts-phase field method to model the simultaneous evolution of microstructure and composition (6). The method couples the Monte Carlo Potts and phase field methods in a way that provides computational efficiency with solution accuracy.

As discussed in the following chapters, the Potts-phase field method, similar to the phase field model, requires a free energy functional to correctly represent material behavior. This task grows more challenging when considering multi-component and multi-phase systems, which are common in today's alloys. Chapter 2 demonstrates the incorporation of phase specific free energy data, contained in thermodynamic databases, into the hybrid Potts-phase field model. The new framework also incorporates thermal diffusion into the model and can be extended to

multi-component systems, allowing alloys with any number of components or phases to be modeled. The application of the framework to the Al-Si system is demonstrated.

Chapter 3 utilizes the Hybrid Potts-phase field method to investigate constituent redistribution in U-Pu-Zr alloys, which is driven by phase changes that result from the thermal gradients in the nuclear fuel. The work details the extension of the recently introduced hybrid Potts-phase field method (6) to ternary alloy systems. The Potts-phase field method, which is capable of simultaneously evolving both the microstructure and composition, utilizes a thermodynamic database of the U-Pu-Zr system (1) to drive the system evolution. The model is first applied to an alloy composition of U-16Pu-23Zr (at%) in order to compare the method results to previous experimental work. The model is then used to investigate the composition and phase evolution of the U-Pu-Zr fuel over the entire compositional spectrum. It is noted that this work represents an important step forward through full ternary modeling of the constituent redistribution in the U-Pu-Zr fuel. The work is intended to provide general trends in the constituent redistribution rather than detailed analysis of specific alloy compositions.

2 HYBRID POTTS-PHASE FIELD MODEL FOR COUPLEDMICROSTRUCTURAL-COMPOSITIONAL EVOLUTION*

2.1 Methods

2.1.1 The Hybrid Potts-Phase Field Method

The hybrid Potts-phase field model is a modeling technique that is capable of simultaneous microstructural-compositional evolution (6). The modeling technique joins the Monte Carlo Potts model, which simulates the microstructure evolution, with the phase field method, which is used to simulate the compositional evolution. While both of these methods have proven particularly useful in modeling various microstructural phenomena, the combination provides a nice balance between resolution and efficiency.

The Monte Carlo Potts model has proved to be an efficient method to evolve large microstructures, including a variety of different phenomena, with the use of a discrete set of particles on a lattice (7). This set of particles represents the microstructure for each site with an integer spin number. This spin number can represent any given microstructural feature, such as grain orientation. Boltzmann statistics are used to systematically attempt spin changes for each site, to one of its neighboring sites. The probability of a site changing its spin is given by,

* The contents of this chapter have been published previously as Ref. (8).

$$P = \begin{cases} \exp\left(-\dfrac{\Delta E}{\kappa_B \cdot T}\right) & \Delta E > 0 \\ 1 & \Delta E \leq 0 \end{cases} \qquad 2\text{-}1$$

where ΔE, is the change in energy associated with a given spin change. In this way, the sites evolve to a lower overall energy by transforming the microstructure and grain boundary network.

The phase field model has proven to be efficient for modeling phase, composition or microstructural evolution, as well as a variety of other phenomena (7). However, the three are not typically coupled due to the complexity of generating an appropriate free energy functional. In practice, the phase field method is a continuum thermodynamic method that utilizes continuum or phase field variables to represent the state of the system at a given point. Kinetic equations, such as the Cahn-Hilliard or Ginzburg-Landau equations, govern the evolution of each phase field in the continuum. These kinetic equations are dependent on a given free energy functional, and thus, the thermodynamics of the system.

The Monte Carlo Potts model is computationally efficient due to the use of a single integer variable at each site and is characterized by sharp interfaces. In contrast, the phase field model can be computationally expensive due to the use of multiple continuum variables with diffuse interfaces. The hybrid Potts-phase field model effectively employs the useful characteristics of the two different methods in a single framework. The Potts method provides efficient representation and evolution of large microstructures, while the phase field method provides the continuum fields necessary to capture composition evolution.

The coupling between the two methods occurs through a free energy functional, which sums the volumetric free energy at a given location with the interfacial free energy terms from the two different methods

$$E_{Hybrid} = \sum_{i=1}^{N}\left(E_v(q_i, C_i) + \sum_{j=1}^{n} J(q_i, q_j) + \kappa_C(\nabla C_i)^2 \right). \quad 2\text{-}2$$

In Eq. 2-2, E_v is the volumetric energy term as a function of both particle state, q_i, and composition, C_i. The interfacial energy terms $J(q_i, q_j)$ and $\kappa_C(\nabla C_i)^2$ are the traditional interfacial energy terms from Monte Carlo Potts and phase field, respectively. The Monte Carlo Potts energy defines grain boundary or phase boundary energy due to differing particle state values (i.e. when neighboring particle states are identical, they have no contribution, and when they are different the interfacial energy is defined equal to the grain or phase boundary energy). The phase field term originates from the Cahn-Hilliard compositional gradient energy (8).

2.1.2 Incorporating a Thermodynamic Database

In the hybrid Potts-phase field model, the composition of the system is evolved using Fick's 2nd law of diffusion,

$$\frac{\partial C_i}{\partial t} = -\nabla \cdot J_i \quad 2\text{-}3$$

where J, the diffusional flux, is defined as,

$$J = -M\nabla\mu. \quad 2\text{-}4$$

Here, M is the mobility and μ is the chemical potential of the constituent. Here, we define μ according to the Cahn-Hilliard approach,

$$\mu = f'(C) - \varepsilon\nabla^2 C \quad 2\text{-}5$$

where f is the free energy density function and $\nabla^2 C$ characterizes the concentration gradient contribution to the interfacial free energy (9) (8). Here, $f'(C)$ is defined as the partial derivative of the Gibbs free energy with respect to the composition,

$$f'(C) = \left.\frac{\partial G}{\partial C}\right|_{T,P}. \qquad 2\text{-}6$$

G can be characterized from a functional or a thermodynamic database where the free energy at any site is the sum of the contributing phases.

$$\begin{aligned} G(C,q) &= q^l G^l + q^\alpha G^\alpha + q^\beta G^\beta + \ldots \\ &= \sum_{p=l,\alpha,\beta,\ldots} q^p G^p \end{aligned} \qquad 2\text{-}7$$

where q is the phase fraction. Defining the free energy this way, Eq. 2-6 becomes,

$$f'(C,q) = \sum_{p=l,\alpha,\beta,\ldots} q^p f'^p \qquad 2\text{-}8$$

where f'^p is obtained by applying Eq. 2-6 to the individual phase, p. Assuming M in Eq. 2-4 is held constant, the time rate change of composition becomes,

$$\frac{\partial C}{\partial t} = M\left[\nabla^2 f'(C) - \varepsilon\nabla^4 C\right] \qquad 2\text{-}9$$

where the second gradient of $f'(C)$ becomes,

$$\nabla^2 f' = \sum_p \left[\nabla^2 q^p * f'^p + 2 * \nabla q^p \cdot \nabla f'^p + q^p * \nabla^2 f'^p\right]. \qquad 2\text{-}10$$

Modeled in this way, the free energies obtained from a thermodynamic database can be incorporated into the Potts-phase field model. It is important to note that although this derivation is to be applied to the Potts-phase field model, it readily applies to phase field methods as well.

2.1.3 2-Component System

In order to incorporate the diffusion of both mass and heat, we review flux in a network-constrained two-component system (10). The following derivation can be readily extended to ternary and higher order systems. These flux equations are defined as

$$
\begin{aligned}
J_1 &= -M_{11}\nabla\left(\mu_1-\mu_2\right)-\frac{M_{1Q}}{T}\nabla T \\
J_2 &= -M_{12}\nabla\left(\mu_1-\mu_2\right)-\frac{M_{2Q}}{T}\nabla T \\
J_Q &= -M_{1Q}\nabla\left(\mu_1-\mu_2\right)-\frac{M_{QQ}}{T}\nabla T
\end{aligned}
\qquad \text{2-11}
$$

where J_1, J_2 and J_Q are the fluxes of the two constituents and the heat flux, respectively. It can be shown that $\sum_j M_{ij}=0$ and $\sum_i M_{ij}=0$ for network constraints. Therefore, for a two-component system, $M_{11}=-M_{12}$, $M_{22}=-M_{12}$ and $M_{11}=M_{22}$. The heat of transport, Q^*, is defined in the absence of a thermal gradient as,

$$
\frac{J_Q}{J_1}=\frac{M_{1Q}}{M_{11}}=Q_1^*. \qquad \text{2-12}
$$

It can be shown that, $Q_1^*=-Q_2^*$. In binary systems, the chemical potentials (ignoring the Cahn-Hilliard term here) of the two components are approximately equal but opposite,

$$
\mu_1=\frac{\partial G}{\partial C_1}\approx-\frac{\partial G}{\partial C_2}=-\mu_2 \qquad \text{2-13}
$$

therefore the difference of the chemical potentials can be simplified to, $\mu_1-\mu_2=2\mu$. The component and heat fluxes in Eq. 2-11 become,

$$
\begin{aligned}
J_1 &= -M_{11}\left(2\nabla\mu+\frac{Q_1^*}{T}\nabla T\right)=-J_2 \\
J_Q &= -2M_{11}Q_1^*\nabla\mu-K\nabla T
\end{aligned}
\qquad \text{2-14}
$$

where the thermal conductivity is defined as $K=M_{QQ}/T$. Inserting the flux equation for component one back into Eq. 2-3, one obtains,

$$
\frac{\partial C_1}{\partial t}=-\nabla J_1=2M_{11}\nabla^2\mu+M_{11}Q_1^*\nabla\cdot\left(\frac{1}{T}\nabla T\right). \qquad \text{2-15}
$$

The evolution of energy, or enthalpy, is related to the time rate change in temperature and is given by

$$\frac{\partial h}{\partial t} = c_p \frac{\partial T}{\partial t} = -\nabla \cdot J_Q = 2M_{11}Q_1^* \nabla^2 \mu + K\nabla^2 T \,. \qquad 2\text{-}16$$

Using the Cahn-Hilliard definition of the chemical potential (Eq. 2-5), the time rate change of composition and temperature respectively become

$$\frac{\partial C}{\partial t} = M_{11}\left[2\left(\nabla^2 f'(C) - \varepsilon\nabla^4 C\right) + Q_1^*\left(\nabla\left(\frac{1}{T}\right)\cdot\nabla T + \frac{1}{T}\cdot\nabla^2 T\right)\right] \qquad 2\text{-}17$$

and

$$\frac{\partial T}{\partial t} = \frac{2M_{11}}{c_p}Q_1^*\left(\nabla^2 f'(C) - \varepsilon\nabla^4 C\right) + \frac{K}{c_p}\nabla^2 T \,. \qquad 2\text{-}18$$

2.2 Results

The incorporation of thermodynamic data into the Potts-phase field method is demonstrated for the Al-Si binary eutectic system. The thermodynamic data for the Al-Si system is obtained from Thermo-Calc software. Figure 2-1 (a) illustrates the phase diagram of Al-Si obtained from the Thermo-Calc software, with an inset of the free energy curves at 500° C. The phase diagram and inset have been overlaid with a color scheme to illustrate the expected phase fractions for a given composition and temperature.

To test the ability of the hybrid Potts-phase field method to capture the expected phase fractions, 600 simulations were run over the composition range of [0,1] and temperature range of [0,1500]° C. The free energy functionals for the three phases of the Al-Si system were exported

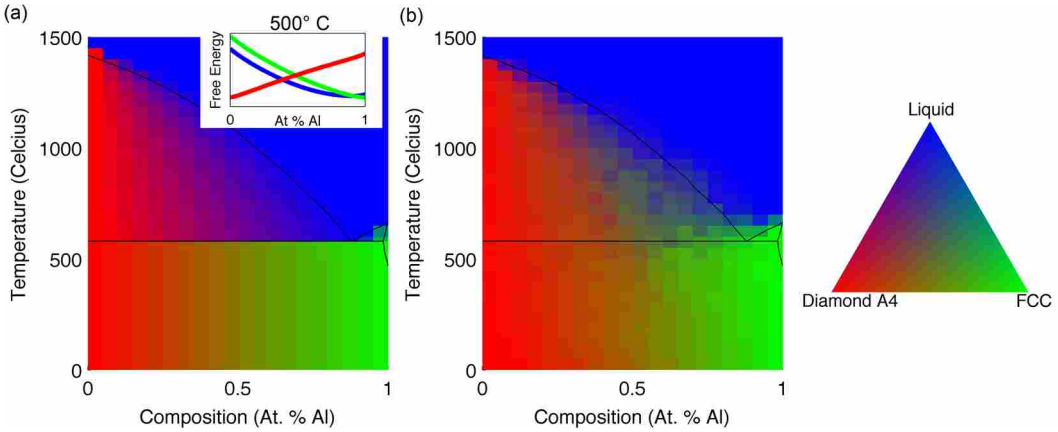

Figure 2-1 Al-Si Phase Diagram Comparison. (a) Thermo-Calc phase diagram and (b) phase fraction resulting from simulations of the Al-Si system. Each is colored according to the triangular legend to illustrate the phase fractions at a given temperature and composition.

from Thermo-Calc and imported into the Potts-phase field application style that has been developed to work with the open source Stochastic Parallel PARticle Kinetic Simulator (SPPARKS) code, maintained by Sandia National Laboratories.

A 2D simulation of 100 x 100 sites was run over 800 Monte Carlo Steps (MCS). Kinetic input parameters, including the mobility, M, Cahn-Hilliard energy, ε, and heat of transport, Q^*, were not readily available for Al-Si and as such were set to arbitrary values. Future work will focus on selecting appropriate values for these quantities to accurately capture the kinetic aspects of the evolution.

shows the evolution of the microstructure, phase, and composition of the system at a temperature of 500° C and an overall composition of 80 at % Al. In all cases, the system started with conditions of randomly assigned phases and spins, but with a uniform composition. As can be seen in , the system quickly evolves the composition to the appropriate values for each phase. Microstructure and phase coarsening occur over time, while tracking the appropriate composition with each phase. The system evolves toward the equilibrium phase

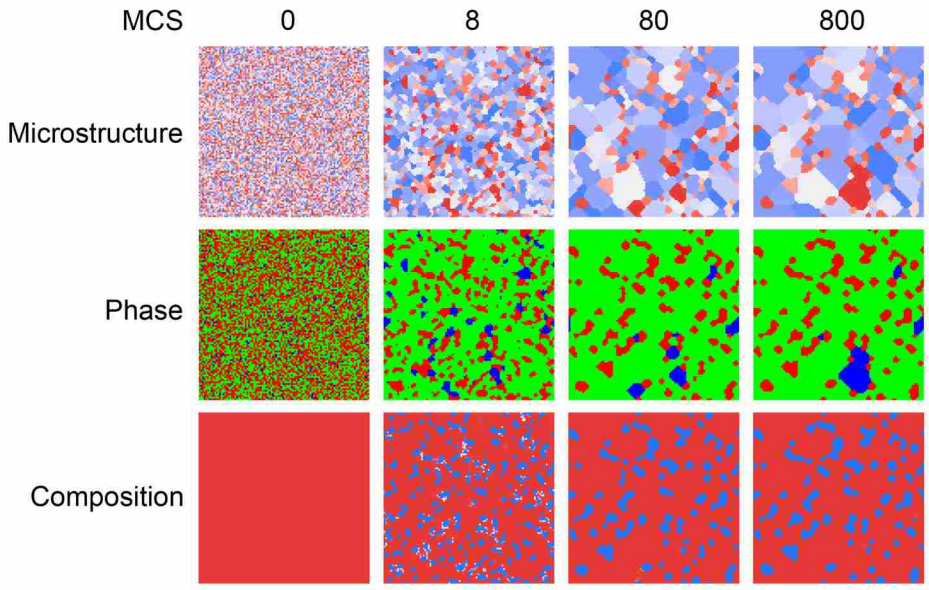

Figure 2-2 - Al-Si Simulated Evolution. Snapshots of the microstructure, phase and composition distributions of the simulation at 500° C and an overall composition of 0.8. Coarsening of the structure can be observed, as well as the trend towards the equilibrium volume fraction of the different phases

fraction expected for the temperature and composition. It is noted, that although the majority of the simulation evolves towards the appropriate phase fraction, there are small pockets of the liquid phase, which is not expected under equilibrium conditions since the eutectic temperature for this alloy is 577° C. However, as can be seen in the inset to Figure 2-1 (a), the reduction in energy due to phase separation of FCC and Diamond A4 phases is small when compared with the free energy of the liquid phase at a composition of 80 at % Al. As such, the reduction in total energy, including creation of new interfaces, may lead to the persistence of the liquid phase. It may also simply be that the initial conditions start with an unusually high fraction of the liquid phase for equilibrium under these conditions.

Similar trends, to the simulation at 500° C and an overall composition of 80 at % Al, were observed in the more than 600 simulations over the range of temperatures and compositions studied. In each case, the simulation trended towards the equilibrium volume fraction. The final volume fraction for all the simulations is plotted in the phase diagram illustrated in Figure 2-1

(b). Here it can be seen that the simulated phase diagram compares well with that obtained from Thermo-Calc. The slight discrepancies between the two are focused in the different two-phase regions where phase separation does not always lead to a significant reduction in energy and as such, one of the non-equilibrium phases persists. In spite of this, the method and use of a thermodynamic database to simulate simultaneous microstructure and composition evolution in a system appears promising.

In the interest of space, the effects of thermal gradients are not demonstrated here. However, the composition and temperature evolution equations, defined in Eqs. 2-17 and 2-18, capture the well-known Soret effect, where mass diffusion can transfer heat through the constituents and induce a thermal gradient by the mass diffusion (9).

3 CONSTITUENT REDISTRIBUTION INVESTIGAED OVER THE COMPOSITIONAL SPECTRUM OF THE U-PU-ZR SYSTEM USING THE POTTS-PHASE FIELD MODELING TECHNIQUE†

3.1 U-Pu-Zr Background

Metal fuels in nuclear reactors have many desirable properties: high thermal conductivity, high fissile and fertile atom density capability, and ease of fabrication (11). However, metal fuels cannot survive the same high temperatures as oxide fuels and, therefore, must operate at lower temperatures. The decreased operating temperature increases the fuel and reactor safety because it limits the diffusion of fusion gas bubbles, containing them within the fuel grains, and allows for a larger margin from the melting temperature. In addition, metal fuels like U-Pu-Zr aid in the long term management of plutonium and other minor actinides.

The U-Pu-Zr alloy also exhibits superior burnup performance in fast reactors and breeder reactors. Zirconium and other elements were initially tested in this alloy as a means to offset the low melting temperature of plutonium. However, zirconium was ultimately chosen because of its unique ability to suppress the interdiffusion of components in the fuel with those of the stainless steel fuel cladding, increasing the safety of the fuel (12). While zirconium successfully increases the liquidus of the alloy, it also increases the solidus. This higher solidus is problematic because of temperature constraints regarding the softening point of the injection casting molds of the fuel rods. Therefore, it was determined that zirconium should be limited to

† The contents of this chapter will be submitted for publication in the Journal of Nuclear Materials.

about 10 wt% for plutonium concentrations up to 20 wt%. During the initial testing of the U-Pu-Zr alloy, three compositions were investigated: U-10Zr, U-8Pu-10Zr, and U-19Pu-10Zr (wt%). Analysis of these alloys showed consistency in the quantity of fission gas released, burnup at which pores became interconnected and anisotropic fuel swelling. Radial redistribution of constituents was expected, and observed, with a seemingly related radial distribution of porosity as well. While limited characterization and performance data is available for the detailed performance of this particular alloy, it is clear that for the commonly investigated compositions, three concentric zones are formed when U-Pu-Zr is irradiated or subject to a thermal gradient, see Figure 1-1 (2). Consistent with previous observations (3), these radially concentric zones show a redistribution of the initially uniform alloy constituents, as well as the resulting inhomogeneity of phases and pore generation. Though metallic fuels have the potential for the highest fissile atom density, the resulting inhomogeneity in U-Pu-Zr alters the achieved fissile atom density and thus the fuel behavior and performance (13).

Securing a better understanding of what drives the constituent redistribution in the U-Pu-Zr alloy is essential to analyzing and predicting its behavior as a nuclear fuel. Previous research has focused on modeling the distribution profiles via numerical methods, learning how material properties affect the models in order to understand experimental results. Ogawa and Iwai numerically solved a one-dimensional Fick's law and hypothesized the effect of including Pu in a U-Zr alloy (14). Ishida et al. extended the Marino model to the U-Pu-Zr system and, by assuming Pu was equally partitioned in U and Zr, defined the system as a quasi-binary system. The resulting model, however, predicted profiles that differed from experimental results and the errors were attributed to temperature predictions that were too high (15).

Further research has attempted to determine the kinetic values of the constituent diffusional coefficients and heat of transports via analytical models. Kim et al. investigated the kinetic and thermo-kinetic properties for irradiated U-Pu-Zr. They calculated the interdiffusion fluxes from experimental test results and used the fluxes to then obtain the interdiffusion coefficients and heats of transport (13). Later work by some of the same authors used a simplified pseudo-binary phase diagram, treating Pu to be immobile, to calculate the redistribution of Zr (16). It is noted that while the use of binary or pseudo-binary systems, as done in the previous work, can yield significant insight, a true ternary modeling of the system would allow a computational investigation of constituent redistribution over all possible alloy composition.

3.2 Methods

3.2.1 Potts-Phase field Method

Simulating constituent redistribution and phase transformations in multi-phase materials like the U-Pu-Zr fuel present a particular challenge. While microstructure and composition are, in reality, interconnected and dependent upon each other, models used to predict microstructural and compositional evolution are often performed separately. Thus, the goal to simulate the U-Pu-Zr system requires the selection of an appropriate materials model. The hybrid Potts-phase field modeling technique has successfully coupled microstructural and compositional evolutions using Potts Monte Carlo and phase field methods, respectively. In short, the Monte Carlo Potts model uses discrete integer values to represent microstructural characteristics, such as grain orientation, phase, etc., while the phase field method uses a continuum variable to simulate the composition.

Recently, the Potts-phase field method was extended to account for thermal diffusion (the Soret Effect) and to incorporate volumetric energy defined by a thermodynamic database (17). The latter has the particular advantage of simplifying simulation for a large range of alloys.

The present work focuses on extending the Potts-phase field framework to ternary alloy systems, so as to model the U-Pu-Zr nuclear fuel. The generalization of the framework to ternary alloys has revealed that extending the modeling framework to higher order alloy systems should be relatively straight forward.

3.2.2 Composition Evolution

The composition of the system is evolved as defined in 2.1.1, with a re-defining of the free energy density function used in Eq. 2-5. The chemical potential is similarly defined according to the Cahn-Hilliard approach (8),

$$\mu_i = \mu_i^* - \varepsilon \nabla^2 C_i \qquad 3\text{-}1$$

where here, μ^* is the partial Gibbs energy (18), also referred to as the homogenous free energy (9), takes the place of *f'(C)* and $\nabla^2 C$ is still the concentration gradient contribution to the interfacial free energy. The reasoning for re-defining the chemical potential in this way will be realized and explained in subsequent sections.

3.2.3 Ternary System

In extending the Potts-phase field method to simulate mass and heat transport in a ternary alloy, special attention was paid to standard methods (10). Thus, according to standard methods, the flux equations for mass and heat transport in a three component, closed, network-constrained system, are given as

$$
\begin{aligned}
J_1 &= -M_{11}\nabla\left(\mu_1-\mu_3\right)-M_{12}\nabla\left(\mu_2-\mu_3\right)-\frac{M_{1Q}}{T}\nabla T \\
J_2 &= -M_{21}\nabla\left(\mu_1-\mu_3\right)-M_{22}\nabla\left(\mu_2-\mu_3\right)-\frac{M_{2Q}}{T}\nabla T \\
J_3 &= -M_{31}\nabla\left(\mu_1-\mu_3\right)-M_{32}\nabla\left(\mu_2-\mu_3\right)-\frac{M_{3Q}}{T}\nabla T \\
J_Q &= -M_{Q1}\nabla\left(\mu_1-\mu_3\right)-M_{Q2}\nabla\left(\mu_2-\mu_3\right)-\frac{M_{QQ}}{T}\nabla T
\end{aligned}
\qquad 3\text{-}2
$$

where J_1, J_2, J_3, and J_Q are the fluxes of the three constituents and the heat flux, respectively. The direct and coupling coefficients between the various driving forces and fluxes are given by the different M_{ij} coefficients. For a closed, network-constrained system one can utilize the following relations,

$$
\sum_j M_{ij} = 0\,,\ \sum_{i=1}^{N_c} J_i = 0\,,\ \sum_i M_{ij} = 0 \qquad 3\text{-}3
$$

as well as the Osager Symmetry Principle (10) to reduce the number of mobility coefficients to the three direct mobility coefficients, i.e. M_{11}, M_{22}, and M_{33} and the M_{1Q} M_{2Q}, and M_{QQ}. The direct coefficient, M_{QQ}, can be replaced by the thermal conductivity according to $K = M_{QQ}/T$ (10), and the coupling coefficients M_{1Q} and M_{2Q} are frequently related to the heat of transport (19).

In order to evolve the temperature in the system, we utilize the relationship between the heat flux and the definition of enthalpy, which gives

$$
\frac{\partial h}{\partial t} = c_p\frac{\partial T}{\partial t} = -\nabla\cdot J_Q \qquad 3\text{-}4
$$

where c_p, is the specific heat (20).

The final partial differential equations controlling constituent and temperature evolution in the system are given by

$$\frac{dC_1}{dt} = M_{11}\left(\nabla^2\mu_1 - \nabla^2\mu_3\right) + \frac{1}{2}(M_{33} - M_{11} - M_{22})\cdot\left(\nabla^2\mu_2 - \nabla^2\mu_3\right) + M_{1Q}\nabla\left(\frac{\nabla T}{T}\right)$$
$$\frac{dC_2}{dt} = \frac{1}{2}(M_{33} - M_{11} - M_{22})\cdot\left(\nabla^2\mu_1 - \nabla^2\mu_3\right) + M_{22}\left(\nabla^2\mu_2 - \nabla^2\mu_3\right) + M_{2Q}\nabla\left(\frac{\nabla T}{T}\right) \quad 3\text{-}5$$
$$\frac{dT}{dt} = \frac{1}{C_p}\left[M_{1Q}\left(\nabla^2\mu_1 - \nabla^2\mu_3\right) + M_{2Q}\left(\nabla^2\mu_2 - \nabla^2\mu_3\right) + K\nabla^2 T\right]$$

where μ is defined according to the Cahn-Hilliard approach in Eq. 3-1.

3.2.4 Incorporating a Thermodynamic Database

Simulation of composition evolution by the phase field method requires the definition of free energy as a function of composition for each phase of interest. This free energy is frequently defined by analytic functionals, but here we elect to utilize a thermodynamic database to achieve a more accurate response for any given alloy, an approach introduced by the authors in (17). In this manner, the framework developed in this work can be applied to any number of alloys, for which the necessary data is available.

In the present work, the free energy at any location is given as the sum of the contributing phases according to a rule-of-mixtures, defined as

$$\begin{aligned} G(C,q) &= q^l G^l + q^\alpha G^\alpha + q^\beta G^\beta + \ldots \\ &= \sum_{p=l,\alpha,\beta,\ldots} q^p G^p \end{aligned} \quad 3\text{-}6$$

where q^p is the phase fraction.

The partial Gibbs energy μ^* for each phase is given (visually) as the value at which a tangent line (or plane or hyper-plane depending upon the order of the alloy) of the free energy intersects the component axes. For a ternary system, this is defined mathematically as

$$\mu_1^*(C_1,C_2)=G(C_1,C_2)+(1-C_1)\left(\frac{\partial G(C_1,C_2)}{\partial C_1}\right)_{C_2}-C_2\left(\frac{\partial G(C_1,C_2)}{\partial C_2}\right)_{C_1}$$
$$\mu_2^*(C_1,C_2)=G(C_1,C_2)-C_1\left(\frac{\partial G(C_1,C_2)}{\partial C_1}\right)_{C_2}+(1-C_2)\left(\frac{\partial G(C_1,C_2)}{\partial C_2}\right)_{C_1} \qquad 3\text{-}7$$
$$\mu_3^*(C_1,C_2)=G(C_1,C_2)-C_1\left(\frac{\partial G(C_1,C_2)}{\partial C_1}\right)_{C_2}-C_2\left(\frac{\partial G(C_1,C_2)}{\partial C_2}\right)_{C_1}$$

where the subscripts refer to the three constituents.

Due to the additive nature of Eq. 3-6, the partial Gibbs energy for each component in a phase just becomes a sum over the appropriate G and $\partial G/\partial C$ terms in Eq. 3-7. However, since both the partial Gibbs energy and the phase fraction can vary in space, the LaPlacian of the chemical potential defined in Eq. 3-1 becomes

$$\nabla^2\mu_i=\sum_p\left[\nabla^2 q^p * \mu_i^{p*}+2*\nabla q^p\cdot\nabla\mu_i^{p*}+q^p*\nabla^2\mu_i^{p*}\right]-\varepsilon\nabla^4 C_i. \qquad 3\text{-}8$$

3.2.5 Implementation

Implementing the Potts-phase field model to simulate constituent redistribution in U-Pu-Zr alloys required the determination of numerous material properties and kinetic constants. In addition, a handful of design decisions had to be made to optimize the accurate simulation of the alloy performance.

The fuel rod performance is simulated in a 2D cross-section with dimensions of 4.32 mm wide, designed to match the diameter of fuel rods in (3, 13), and 2.16mm high. This region is mapped onto a discretized system of 100 by 50 sites. The simulations are fully periodic with the exception that one thermal boundary condition described below. Each site has an area of a^2, where a is the simulation diameter divided by the number of sites, 4.32mm/100 sites or

0.0432mm. For volumetric energy calculations, the simulation is quasi-3D and each site is given a depth of a, resulting in a volume of a^3.

The Gibbs energy for this work utilizes the thermodynamic database developed by Kurata et al. for the U-Pu-Zr system (1). The database follows the standard CALculation of PHase Diagrams (CALPHAD) approach for the 14 phases of this alloy found in the database.

While it is possible, to directly connect the software to Thermo-Calc, or use the analytic functions to calculate the energies during the course of the simulation, it was determined that a tabulated form would be the most efficient and provide the most flexibility for the future implementation of other alloys systems. For this work, a table of Gibbs free energy values is loaded as a function of composition in 0.01 at% steps and temperatures ranging from 768 to 998 K in 5 K steps. The partial Gibbs energy, μ^*, for each constituent is also tabulated. During the simulation, values of G and μ^* are interpolated from the tables using three dimensional linear interpolation.

Occasionally, terminal phases do not exhibit a minimum in the free energy surface near the terminal composition (i.e. $\partial^2 G/\partial C^2 \neq 0$), rather the energy has a minimum value at the terminal composition but still has a non-zero slope at this point ($\partial G/\partial C \neq 0$). This is problematic for numerical simulations because the non-zero slope can drive the composition to values that are unphysical (e.g. negative or greater than unity). Any attempts to correct these values leads to conservation of mass problems in the surrounding sites. To correct this, a quadratically increasing Gibbs energy is simply applied to all composition values that are unphysical, thereby driving the system back to realistic compositions for the terminal phase. For a few terminal compositions, the combination of the non-zero slope ($\partial G/\partial C \neq 0$) and the quadratic correction resulted in a 'miscibility gap' of sorts, leading a single-phase region with two compositions.

Fortunately, these terminal systems are not of particular interest in the alloy development of the U-Pu-Zr system discussed here. Furthermore, future work will eliminate these artifacts by requiring continuity of the correction term with the thermodynamic data.

The phase fraction for all sites, q_i, is defined only using ones and zeros. In other words, each site in the simulation only ever has one phase present.

Material properties for the U-Pu-Zr system are determined as follows. The thermal conductivity and specific heat, given for each constituent in Table 3-1, are averaged during evolution calculations, by taking a compositionally weighted average. The Potts interface (grain boundary) energy is set to 0.2 J/m^2 (21) and the Cahn-Hilliard energy term, ϵ, is set to unity, similar to other work (9), and the higher order Cahn-Hilliard energy terms were calculated according to methods described in (22). It is noted that the Cahn-Hilliard contribution to the evolution of the simulations in this work is typically small.

The molar Gibbs free energy, Potts interface energy, and Cahn-Hilliard energy values are calculated as extensive quantities rather than densities by multiplying the appropriate volumetric, molar or specific values by the appropriate volume/area/mass associated with each site. It is noted that due to scaling and numerical precision issues between volumetric and areal quantities (cubic vs. quadratic), discretization size plays an important role. Thus, to ensure that both the Gibbs free energy and the Potts interface energy contribute to the evolution of the system, the Potts interface energy was scaled by a factor of 10^4, although it was confirmed that smaller discretizations, not used for computational expense, did not require any scaling to ensure equal contribution.

Table 3-1 – Material Property and Diffusivity (Kim et al. (6)) Values for U, Pu, and Zr

Constituent	Direct Diffusivity (10^{-15} m^2/s)	Thermal Diffusivity (10^{-13} m^2/s)	Thermal Conductivity (W/m-K)	Specific Heat (J/kg-K)
U	13.833	2.56	27.5	120
Pu	9.30	-1.10	6.74	130
Zr	12.633	-9.466	22.6	270

Kinetic quantities required to simulate the U-Pu-Zr system are defined as follows. Values for the diffusivities of each constituent are obtained from the results of previous research (13), in which constituent diffusivities were calculated for each of the three concentric zones. Since this model assumes constant values of M, all phases must use the same values. It was determined to use an average of the diffusivities of each constituent from (13). These values are given in Table 3-1. The direct mobility terms are calculated from the averaged diffusivities according to

$$M_{ii} = \frac{D_{ii}}{K_B \cdot T_{Ave}} \qquad 3\text{-}9$$

where K_B is the Boltzmann Constant and T_{Ave} is the average temperature across the simulation (again required because M must be constant for each step).

As a means to simulate the correct grain growth rate, a grain boundary mobility term is used to convert the probability of GB motion by the Monte Carlo Potts model (Eq. 2-1), to a rate. The GB mobility for this work was set to 0.001, which resulted in GB velocities in the range of 10^{-6} m/s, in the range of experimental results (23). As seen in previous work, the K_BT value in the Potts model (Eq. 2-1) is critical to preventing grain growth stagnation (6), and was set accordingly for this work.

To simulate the thermal gradients that drive so much of the phase and constituent evolution, a temperature profile similar, but not exact, to that described in (13) was utilized. This profile was obtained and maintained in a steady state by constantly adding heat to all the sites in the model. The addition of this heat, in combination with the boundary condition that the

outermost sites are maintained at 823 K, resulted in a quadratically shaped (negative curvature) temperature profile with a peak temperature of 943 K.

The simulation was tracked over 80,000 Monte Carlo steps (MCS), with 100 sweeps of the concentration field for each MCS. All hybrid Potts-phase field model simulations are performed using the **S**tochastic **P**arallel **PAR**ticle **K**inetic **S**imulator (SPPARKS). SPPARKS is an open source, parallelized Monte Carlo code for on/off lattice models maintained by Sandia National Laboratories (24) (25), for which a hybrid Potts-phase field application style was created (6).

3.3 Simulation Results and Discussion

3.3.1 Comparison to U-16Pu-23Zr (at%)

As a means to benchmark the ternary phase and composition modeling of U-Pu-Zr alloys, a system composition of U-16Pu-23Zr (at%) is simulated. This initial composition is chosen in order to compare to detailed results published by Kim et al. (13). The initial conditions for phase fraction and phase composition are determined from the isothermal phase diagram. At 823 K, the low temperature for the simulations, the equilibrium phases, phase fractions and compositions are δ and ζ at 27% and 73% and U-10Pu-70Zr and U-18Pu-6Zr (at%), respectively. To encourage phase transformations, nucleation of all possible phases is attempted for 0.001% of every attempted Potts spin change. While this leads to the attempted nucleation of many phases, the energetic cost of nucleating non-equilibrium phases cause the majority of these nucleation events to disappear in the subsequent sweep. Only the energetically favorable phases nucleate and persist.

Figure 3-1 shows the evolution of grains, phases, phase fractions, composition, average constituent composition, and temperature profile for this system, with the left and right edges

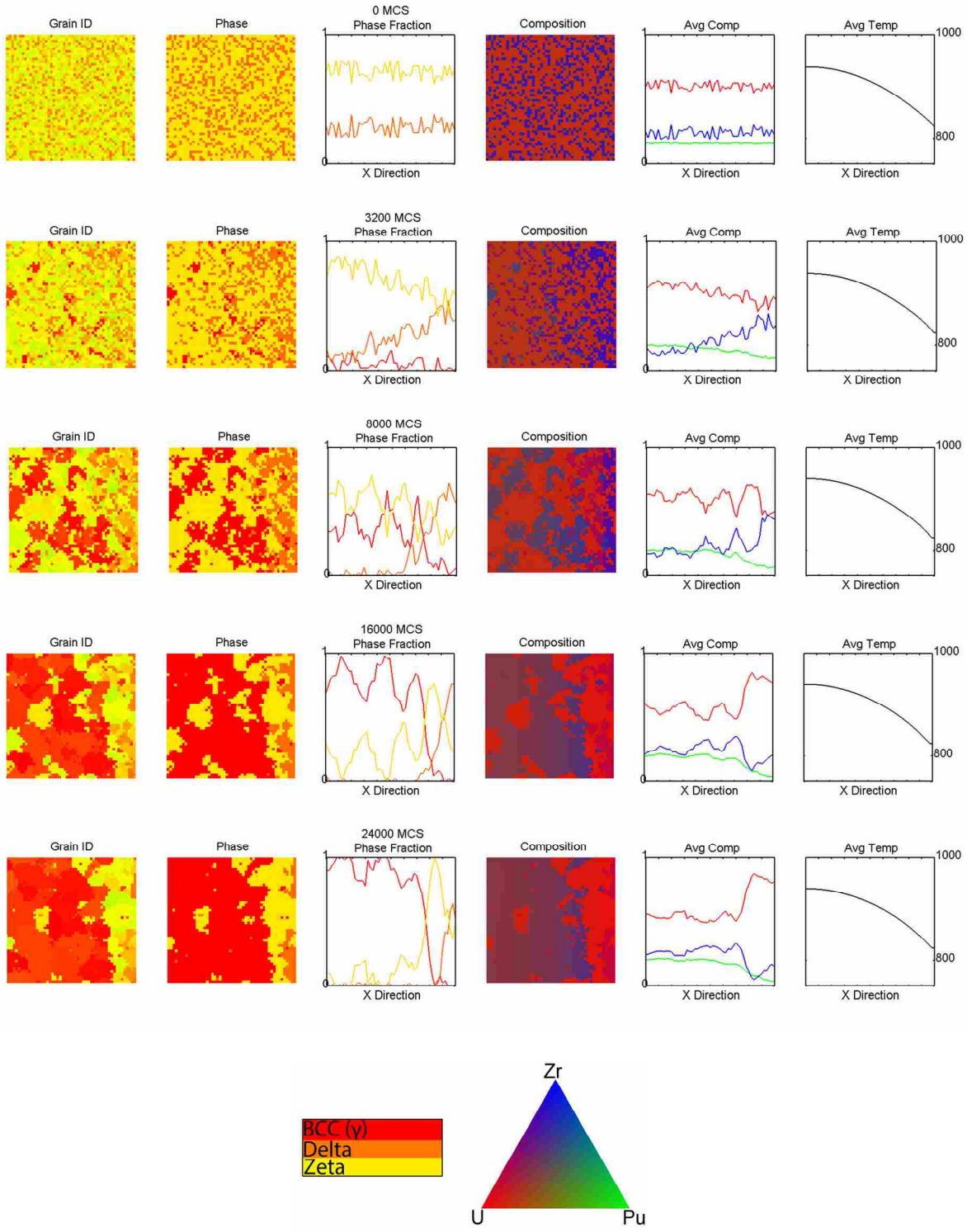

Figure 3-1 U-16Pu-23Zr (at%) Simulated Evolution. Microstructural, phase field (and fraction), compositional (overall and average), and temperature profiles are shown for the U-16Pu-23Zr alloy at various steps throughout the course of evolution. Regions consistent with the experimentally demonstrated concentric zones are observed.

representing the fuel center and fuel surface, respectively. The entire diameter of the fuel rod was simulated, but the image is cut in half due to space limitations in the figure.

The evolution profiles of this simulation show direct similarities to those presented by Kim et al. (13), where the three concentric zones can be observed. The BCC-γ phase nucleates and becomes the dominant phase in the high temperature, center region, while δ and ζ remain in the lower temperature, outer region, with an intermediate γ-ζ region. Likewise, the composition profiles show a Zr-enriched U-depleted center, U-enriched Zr-depleted intermediate region, and the outer region containing the remaining portion of the fuel. This redistribution of constituents accurately predicts the diffusion of zirconium both up and down the temperature gradient, i.e. towards both the fuel center and surface, which is observed in experiments (26). Minimal plutonium redistribution is also shown, with a slight decrease in composition from fuel center to surface, as observed in experiments (27).

It is noted, however, that the average composition of the three concentric zones in the simulations do not replicate those in experimental work (4), as seen in the smoothed composition profiles in Figure 3-2. The intermediate ζ-γ region in the simulation contains a significantly lower volume fraction of uranium rich ζ than in experimental testing, with an almost entirely ζ region near the surface. This shift of the high ζ volume fraction region towards the fuel surface, is somewhat similar to the model created by Kim et al. (16), who attribute the discrepancy to differences in the temperature profile used. We attribute our discrepancies to two factors: a temperature profile that further accentuates the shrinking of the outermost zone and the averaged diffusivities (not phase specific) used in the calculations.

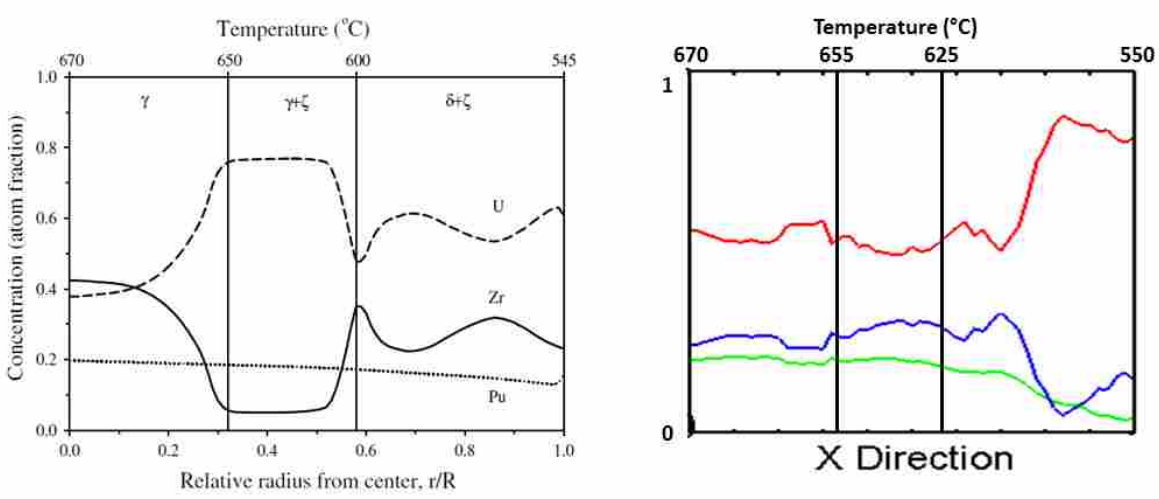

Figure 3-2 – Comparison of Constituent Redistribution Profiles. (Left) Experimental constituent redistribution profiles as interpolated and smoothed by Kim et. al. 2004. (Right) Simulated average constituent redistribution profile after 24,000 MCS.

The temperature profile used was approximate and was not identical to the profile used by Kim et al. (13). More importantly, the profile is not a duplicate of that actually experienced during irradiation, where pore formation and the resulting inhomogeneity of thermal conductivity can have a significant effect on the temperature profile and corresponding phases that emerge. Still, the zone boundaries shown in Figure 3-2 are quite sharp, confirming the unique relationship between temperature and the observed phases found in U-Pu-Zr alloys.

The other factor affecting the imperfect match with experiments relates to the way constituent mobilities are defined. As described in Section 3.2.5, the mobility terms used in this model are averaged from the values for each experimentally measured concentric zone. It is recognized that for the most accurate results, mobility terms for each constituent in each phase would be required. For a majority of the phases present in this alloy, these diffusion values are not known. Therefore, because of both the mathematical definitions and the lack of data, this work assumes the diffusivities to be equal in all phases. Per this assumption, the values are effectively either higher or lower than the actual diffusivities, depending on the specific phase.

Depending on the severity of the incorrect diffusivities, not only could the rate of constituent redistribution be increased or decreased, thus accelerating or decelerating evolution, but the direction of the component flux could also be reversed. This alone would have a significant influence on determining the location of the zone boundaries observed. In order to demonstrate a more realistic evolution of this system, diffusivities specific to every single-phase would be required. At present, diffusivities for the most common phases/phase regions are available (13), but the rest remain unknown.

Differences were observed between experimentally obtained constituent profiles and the thermodynamic database utilized for this work. Specifically, experimentally observed phases, at given compositions and temperatures, were not always consistent with the phase diagrams calculated by the database. In fact, Kim et al. adjusted their pseudo binary phase diagram to correct differences in phase region boundaries to more accurately match the experimentally observed zone boundaries (16). Upon detailed examination of Figure 3-1, it could be suggested that the intermediate zone is transforming into a single-phase ζ region, rather than a δ-ζ or ζ-γ two-phase region. This observation is consistent with predictions based on the equilibrium phase diagram and demonstrates the nature of the modeling technique used. Modeled in this way, the simulations results, while not entirely consistent with experimental results, are consistent with the database used. Thus, the simulation technique reliably returns results consistent with the thermodynamic input.

In summary, the modeling technique shows the same trends in constituent redistribution and phase transformations as published work and even though it is not exact, the simulation results match the database inputs very well.

3.3.2 Survey of Composition Spectrum

Having established the ability of the model to capture the critical trends of constituent redistribution and phase transformation, the entire compositional spectrum of U-Pu-Zr is investigated. This is done by varying composition of U, Pu and Zr in 20 at% steps, according to the compositions of the 21 alloys detailed in Table 3-2. The initial conditions for these simulations differ from those in the U-16Pu-23Zr (at%) benchmark, in that each site is assigned a randomly selected phase and given a composition equal to the overall composition (i.e. the initial composition is uniform). This ensures that all phases are initially present and that results are not dependent on phase nucleation, offering equal opportunity for each phase to persist.

Table 3-2 - 21 Simulated U-Pu-Zr Alloys

Simulation #	U	Pu	Zr	Simulation #	U	Pu	Zr	Simulation #	U	Pu	Zr
1	0.0	0.0	1.0	8	0.2	0.2	0.6	15	0.4	0.6	0.0
2	0.0	0.2	0.8	9	0.2	0.4	0.4	16	0.6	0.0	0.4
3	0.0	0.4	0.6	10	0.2	0.6	0.2	17	0.6	0.2	0.2
4	0.0	0.6	0.4	11	0.2	0.8	0.0	18	0.6	0.4	0.0
5	0.0	0.8	0.2	12	0.4	0.0	0.6	19	0.8	0.0	0.2
6	0.0	1.0	0.0	13	0.4	0.2	0.4	20	0.8	0.2	0.0
7	0.2	0.0	0.8	14	0.4	0.4	0.2	21	1.0	0.0	0.0

Figure3-3 shows the evolved phase map, after 24,000 MCS, overlaid with the average constituent composition for the 21 simulations. The sequential evolution images, similar to Figure 3-1, for each of these simulations can be found in Appendix A. It is noted that a few terminal compositions (pure element or binary alloys) lead to artifacts because the diffusional flux drives the system to unphysical compositions. As mentioned previously, this is a natural consequence of the thermodynamic driving forces at the terminal compositions.

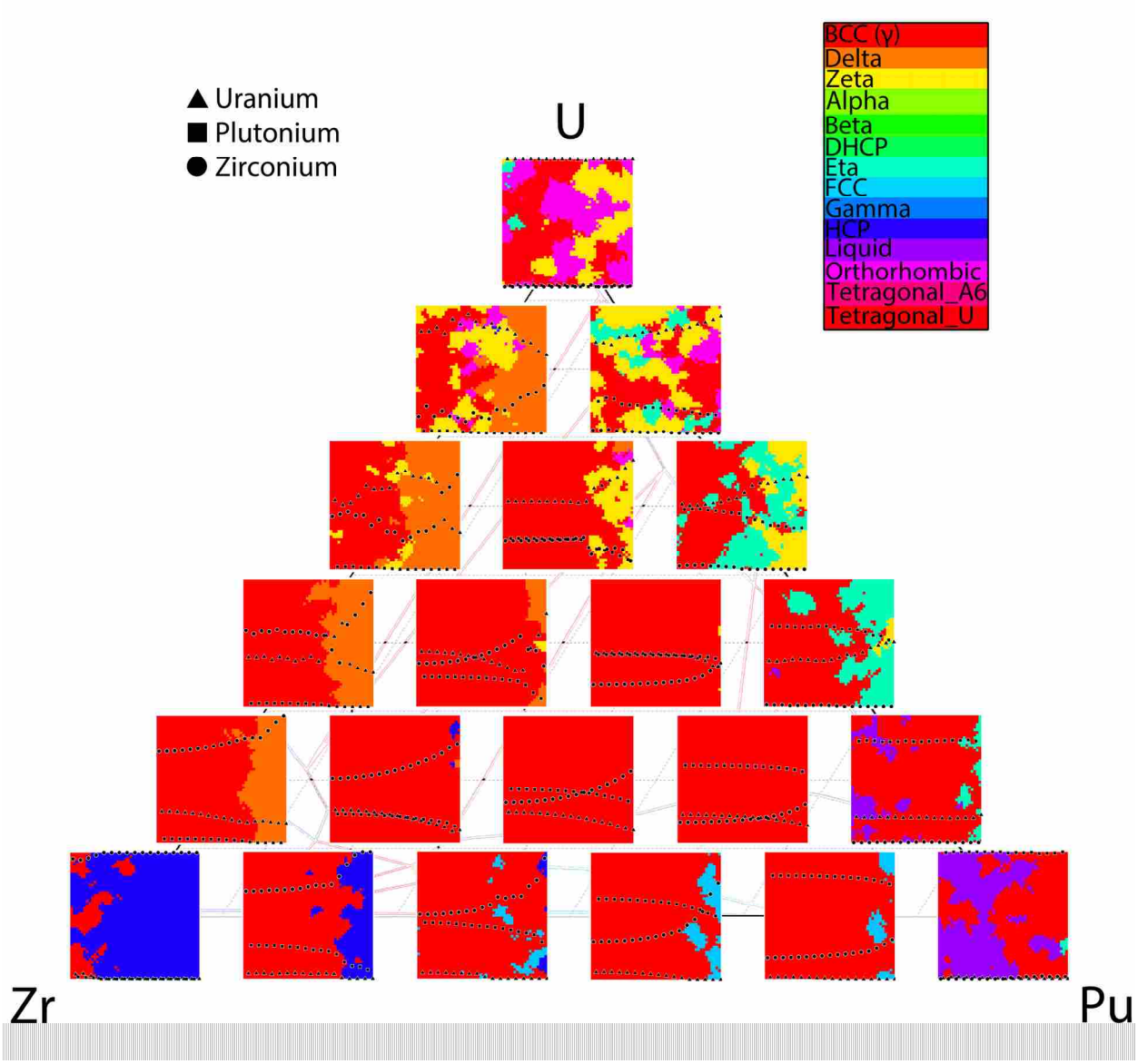

Figure 3-3 - U-Pu-Zr Simulations over Compositional Spectrum. 21 alloy simulations of varying initial compositions after 24,000 MCS are shown. Phase field maps overlaid with average composition profiles reveal constituent redistribution and phase regions formed.

If one studies Figure 3-3 carefully, the phase diagram beneath the images can be seen in the microstructure, both in phase fraction and composition. This is the first indication that the simulation technique captures the appropriate behaviors.

In an effort to validate the results of this survey, we compare our results to a recent study by Burkes et al. (2). In this work, Burkes et al. determine the phase transition temperatures of

several U-Pu-Zr alloys, namely, U-24Pu-15Zr, U-36Pu-20Zr, U-39Pu-20Zr, U-34Pu-30Zr, U-35Pu-30Zr, U-29Pu-40Zr, all in wt%. These alloys can be compared, most closely, to either simulation 13 (U-20Pu-40Zr at%) or simulation 17 (U-20Pu-20Zr at%) for the first three alloys and simulation 8 (U-20Pu-60Zr at%) for the other three alloys. By comparison, the results are consistent with Burke's findings for two of the three transition temperatures. For example, the $\zeta + \gamma \rightarrow \delta + \zeta + \gamma$ and $\delta + \zeta + \gamma \rightarrow \delta + \zeta$ transitions, which occur in the first three alloys, are within the temperature ranges given by Burkes. However, the $\gamma \rightarrow \zeta + \gamma$ transition in the simulation occurred at a noticeably lower temperature, 40-50 K, than that found by Burkes et al.(2). This lower simulated $\gamma \rightarrow \zeta + \gamma$ transition temperature is attributed to the same discrepancies detailed in Section 3.3.1 where the γ region extends closer to the surface than experimental results, but is consistent with the thermodynamic input.

3.3.3 Alloy Development

Upon further examination of Figure 3-3 it is clear that significant constituent redistribution occurs in U-Pu-Zr alloys over a wide range of overall composition. Nevertheless, careful selection of alloy composition can significantly reduce the amount of redistribution that occurs. Obviously, little to no constituent redistribution will occur in pure, or nearly pure, substances, such as simulations 1, 6 and 21. However, simulations 2,5,7,10,11, and 14 also showed little redistribution.

As described previously, alloys rich in plutonium have unacceptably low melting temperatures. Likewise, zirconium rich alloys have unacceptably high solidus temperatures. Therefore, an ideal alloy will successfully compromise the two offsetting characteristics. As shown in Figure 3-4, the majority of tested alloys are within the acceptable range of compositions.

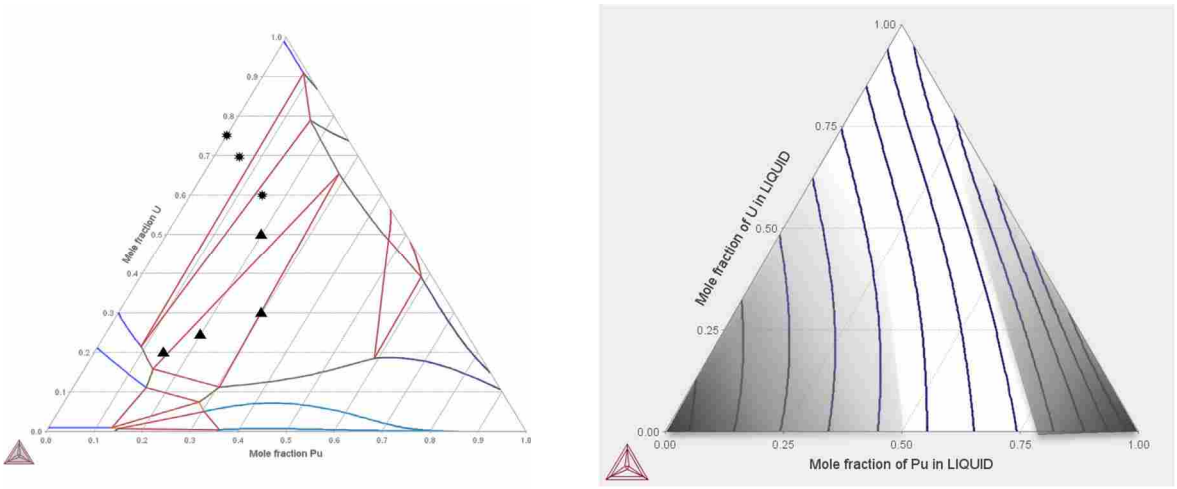

Figure 3-4 - Alloy Development. (Left) Previously tested alloys (* - Phal et. al. 1986 (4). ▲ - Burkes et. al. 2010 (2)). (Right) Range of acceptable U-Pu-Zr alloy compositions, offsetting plutonium's low melting temperature with zirconium's high solidus temperature.

Previous work has documented that highly distorted microstructure and large cavities, due to "tear-like" porosity, are seen between grain boundaries, as well as phase boundaries within grains, primarily in the outer most δ inhabited regions (28). It could be proposed that uniformity of phase throughout the fuel rod would reduce the distorted tearing of the microstructure. When considering the constraints placed on the amount of zirconium in relation to plutonium content, of the alloys showing limited redistribution, the U-40Pu-20Zr (at%) alloy (simulation 14) exhibits uniformity of phase, consisting almost entirely of the γ phase. The mostly γ phase map of simulation 14 suggest that a homogeneity of phase, and the corresponding decrease in the high surface area δ –lamellae, may be possible for fuel rods in the U-Pu-Zr alloy.

Fuel performance and attained burnup percentages can be improved by maintaining uniformity of phase and compositions across the fuel rod. By sustaining an even distribution of constituents, U-40Pu-20Zr (at%) alloys will preserve a consistent dispersal of fissile atoms, thus limiting localized hot spots that result from concentrated fissile atoms densities. Additionally,

reducing phase boundary area by maintaining a homogenous phase will likely decrease pore generation and microstructural tearing, further improving fuel performance.

4 CONCLUSIONS

4.1 Hybrid Potts-Phase Field Modeling Method

Extensions of the hybrid Potts-phase field model capture thermal diffusion and allow readily available, material specific thermodynamic databases to be utilized. The use of a thermodynamic database opens the method to a variety of multi-component alloys. The method developments are demonstrated for the Al-Si binary system. Alloy evolutions to appropriate phase fractions and composition convey a good match between the simulated and analytical phase diagrams, thus validating the method expansions.

4.2 U-Pu-Zr Nuclear Fuel Alloys

The hybrid Potts-phase field method has been promoted to simulate constituent redistribution and phase transformations in three-component systems. Validation of the modeling developments is performed by comparing simulation results with experimentally examined fuel rods of U-16Pu-23Zr (at%). The evolved phase regions and constituent redistribution results are generally in line with the irradiated alloy. However, it is clear that the simulated ζ dominant, uranium rich, intermediate region is much closer to the fuel surface than in experimental tests. The disagreements between simulation and experiment are attributed to the models use of constant diffusivities and an inexact thermal profile.

The effects of initial alloy composition are investigated by modeling fuel evolution over the entire range of U-Pu-Zr compositions. The U-40Pu-20Zr (at%) alloy shows the most potential to remain homogenous, in both phase and compositions, throughout a thermal gradient over the applicable temperature range. Other simulated alloys, within the acceptable range of plutonium and zirconium compositions, demonstrated significant constituent redistribution and/or extensive phase transformations, both undesirable behaviors that limit fuel performance.

The greatest challenges to accurately modeling the U-Pu-Zr system are related to balancing the simplicity of the model with the need to capture complex material specific phenomena. The lack of exact material properties, thermodynamic data and kinetic quantities, specific to the phases of U-Pu-Zr system, amplify the complexity of modeling the system with this method. However, the present work consistently matches the input data, indicating the need for improved input parameters. Specifically, accurate component diffusivity values, unique for each critical phase, ideally for all phases, and a temperature profile equivalent to experimental tests would notably increase the fidelity of this model.

REFERENCES

1. Kurata, M., *IOP Conference Series: Materials Science and Engineering* **2010,** *9* (1), 012022.

2. Burkes, D. E.; Kennedy, J. R.; Hartmann, T.; Papesch, C. A.; Keiser Jr, D. D., *Journal of Nuclear Materials* **2010,** *396* (1), 49-56.

3. Murphy, W.F.; W. N. B.; Brown, F.L.; Koprowski, B.; Neimark, L.A., *Argonne National Laboratory* **1969,** *Report ANL-7602*.

4. Pahl, R. G., Lahm, C.E., Villareal, R, Beck, W.N., Hofman, G.L., *International Conference on Reliable Fuels for Liquid Metal Reactors* **1986**.

5. Humphreys, F. J.; Hatherly, M., Chapter 8 - Recrystallization of Ordered Materials. In *Recrystallization and Related Annealing Phenomena (Second Edition)*, Humphreys, F. J.; Hatherly, M., Eds. Elsevier: Oxford, 2004; pp 269-283.

6. Homer, E. R.; Tikare, V.; Holm, E. A., *Computational Materials Science* **2013,** *69* (0), 414-423.

7. Miodownik, M., 3 - Monte carlo potts model. In *Computational Materials Engineering*, Janssens, K. G. F.; Raabe, D.; Kozeschnik, E.; Miodownik, M. A.; Nestler, B., Eds. Academic Press: Burlington, 2007; pp 47-108.

8. Cahn, J. W.; Hilliard, J. E., *The Journal of Chemical Physics* **1958,** *28* (2), 258-267.

9. Zhang, L.; Tonks, M. R.; Millett, P. C.; Zhang, Y.; Chockalingam, K.; Biner, B., *Computational Materials Science* **2012,** *56* (0), 161-165.

10. Balluffi, R. W.; Allen, S. M.; Carter, W. C., Driving Forces and Fluxed For Diffusion. In *Kinetics of Materials*, John Wiley & Sons, Inc.: 2005; pp 41-76.

11. Mohr, D.; Chang, L. K.; Feldman, E. E.; Betten, P. R.; Planchon, H. P., *Nuclear Engineering and Design* **1987,** *101* (1), 45-56.

12. Hofman, G. L.; Walters, L. C.; Bauer, T. H., *Progress in Nuclear Energy* **1997,** *31* (1–2), 83-110.

13. Kim, Y. S.; Hofman, G. L.; Hayes, S. L.; Sohn, Y. H., *Journal of Nuclear Materials* **2004,** *327* (1), 27-36.

14. Marino, G. P., *Nuclear Science and Engineering* **1972,** *49* (1), 93-98.

15. Ishida, M; Kinoshita, M.; T.O., *Nuclear Technology* **1993,** *104*, 37.

16. Kim, Y. S.; Hayes, S. L.; Hofman, G. L.; Yacout, A. M., *Journal of Nuclear Materials* **2006,** *359* (1–2), 17-28.

17. Cox, J. J.; Homer, E. R.; Tikare, V., *MRS Online Proceedings Library* **2013,** *1524*, null-null.

18. Hillert, M., *Phase Equilibria, Phase Diagrams and Phase Trasnformations: Their Thermodynamic Basis*. 2nd ed.; Cambridge University Press: 2008; p 510.

19. Shewmon, P. G., *Diffusion in solids*. McGraw-Hill: 1963.

20. Balluffi, R. W.; Allen, S. M.; Carter, W. C., Irreversible Thermodynamics: Coupled Forces and Fluxes. In *Kinetics of Materials*, John Wiley & Sons, Inc.: 2005; pp 23-39.

21. Shibuta, Y.; Sato, T.; Suzuki, T.; Ohta, H.; Kurata, M., *Journal of Nuclear Materials* **2013,** *436* (1–3), 61-67.

22. Cogswell, D. A.; Carter, W. C., *Physical review. E, Statistical, nonlinear, and soft matter physics* **2011,** *83* (6 Pt 1), 061602.

23. Gottstein, G.; Shvindlerman, L. S.; Zhao, B., *Scripta Materialia* **2010,** *62* (12), 914-917.

24. SPPARKS website. http://spparks.sandia.gov/.

25. Plimton, S.J.; C. C. B., M. Chandross; Holm, E.A.; Thompson, A.; Tikare, V.; Wagner, G.; Webb, E.; Zhou, X., *Sandia National Laboratories* **2009**, 1-82.

26. Pahl, R. G.; Porter, D. L.; Lahm, C. E.; Hofman, G. L., *MTA* **1990,** *21* (7), 1863-1870.

27. Sohn, Y. H.; Dayananda, M. A.; Hofman, G. L.; Strain, R. V.; Hayes, S. L., *Journal of Nuclear Materials* **2000,** *279* (2–3), 317-329.

28. Yun, D.; Rest, J.; Hofman, G. L.; Yacout, A. M., *Journal of Nuclear Materials* **2013,** *435* (1–3), 153-163.

APPENDIX A. 21 U-PU-ZR ALLOY SIMULATIONS

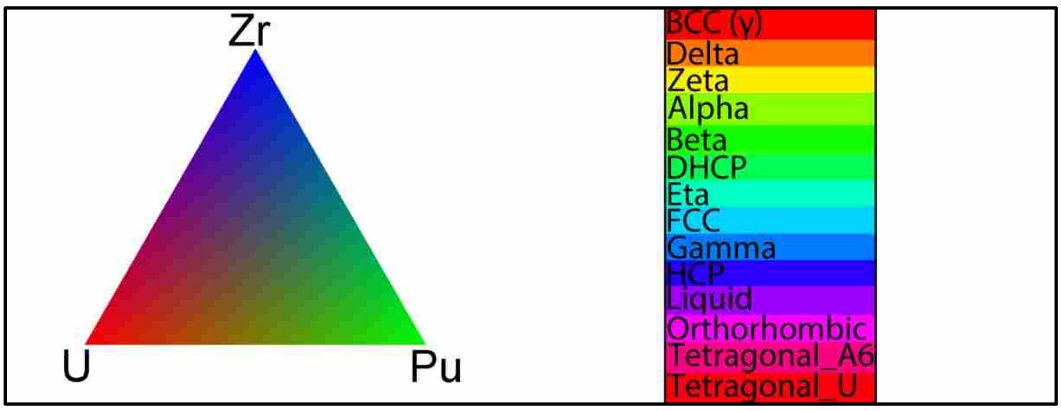

Figure A-1 Master Legend

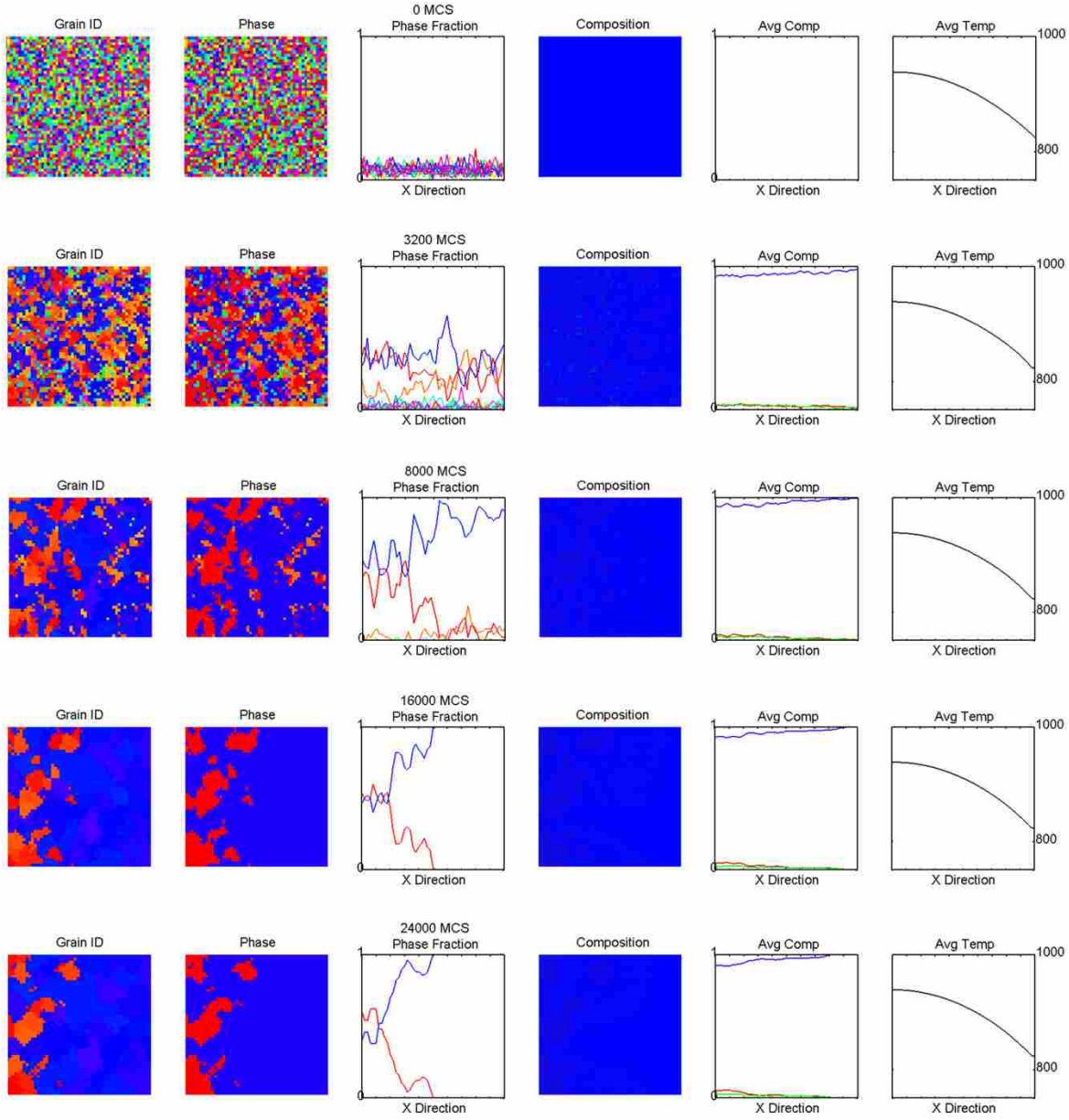

Figure A-2 Simulation 1 (Zr)

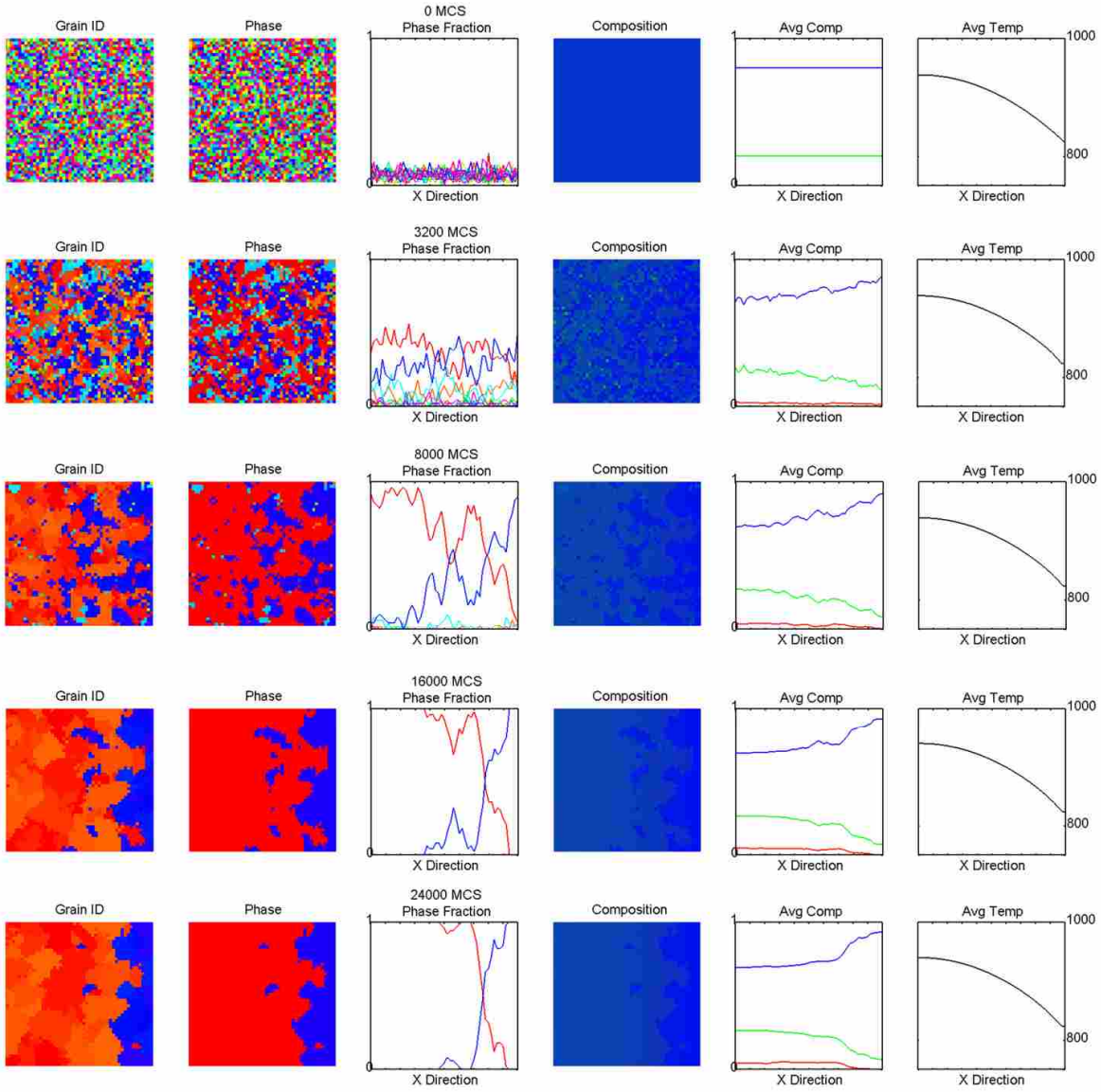

Figure A-3 Simulation 2 (Pu-80Zr)

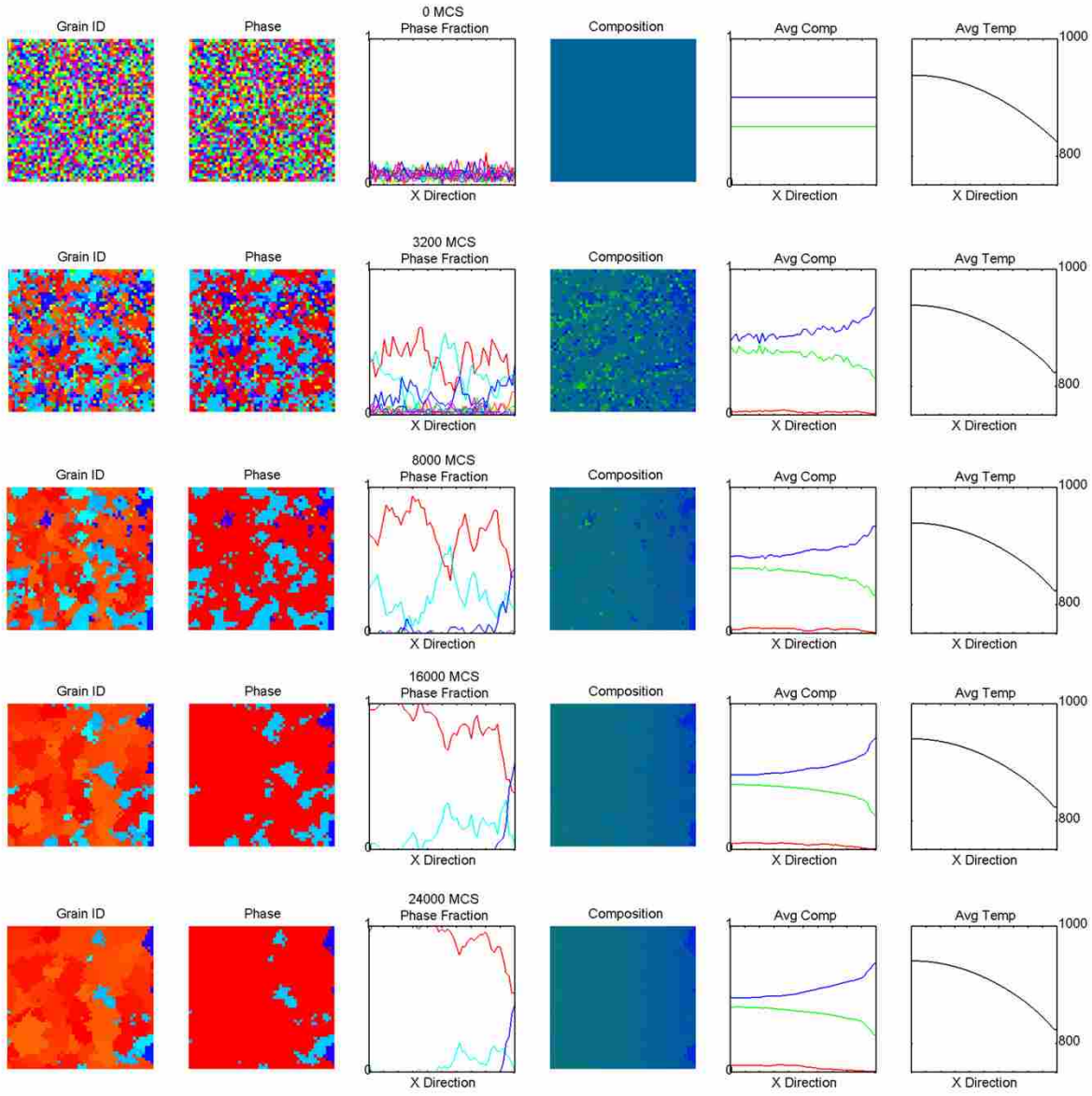

Figure A-4 Simulation 3 (Pu-60Zr)

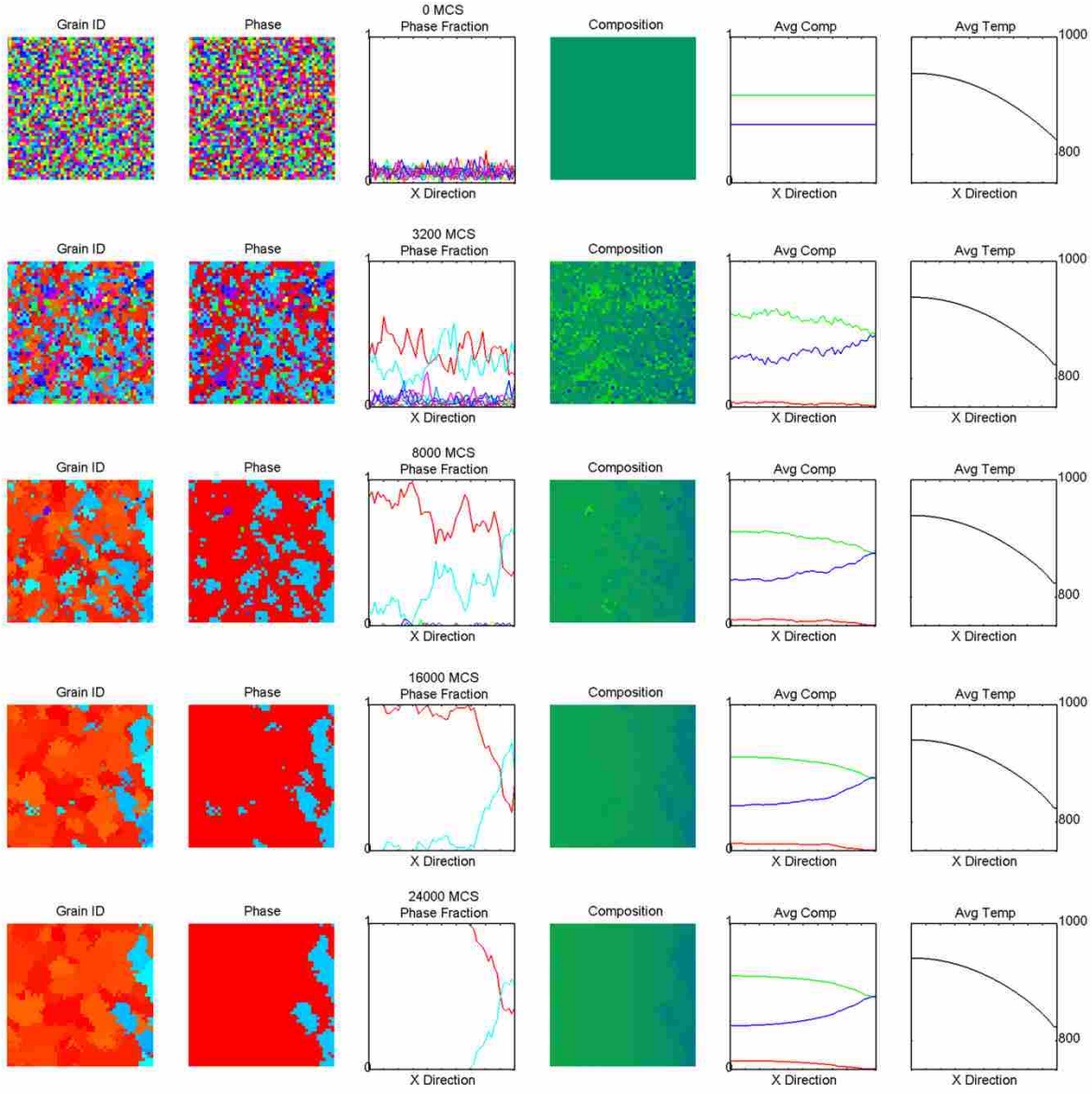

Figure A-5 Simulation 4 (Pu-40Zr)

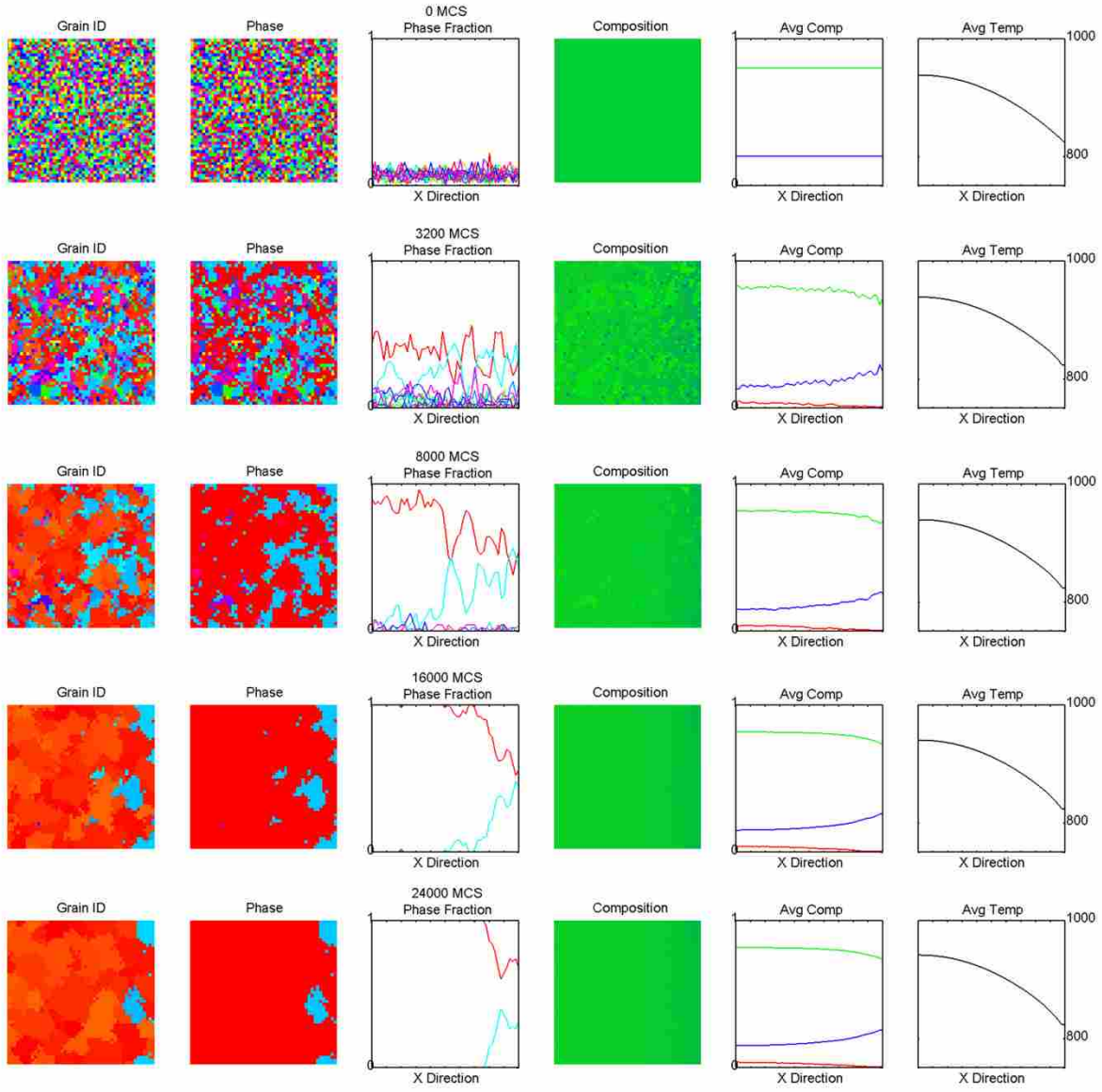

Figure A-6 Simulation 5 (Pu-20Zr)

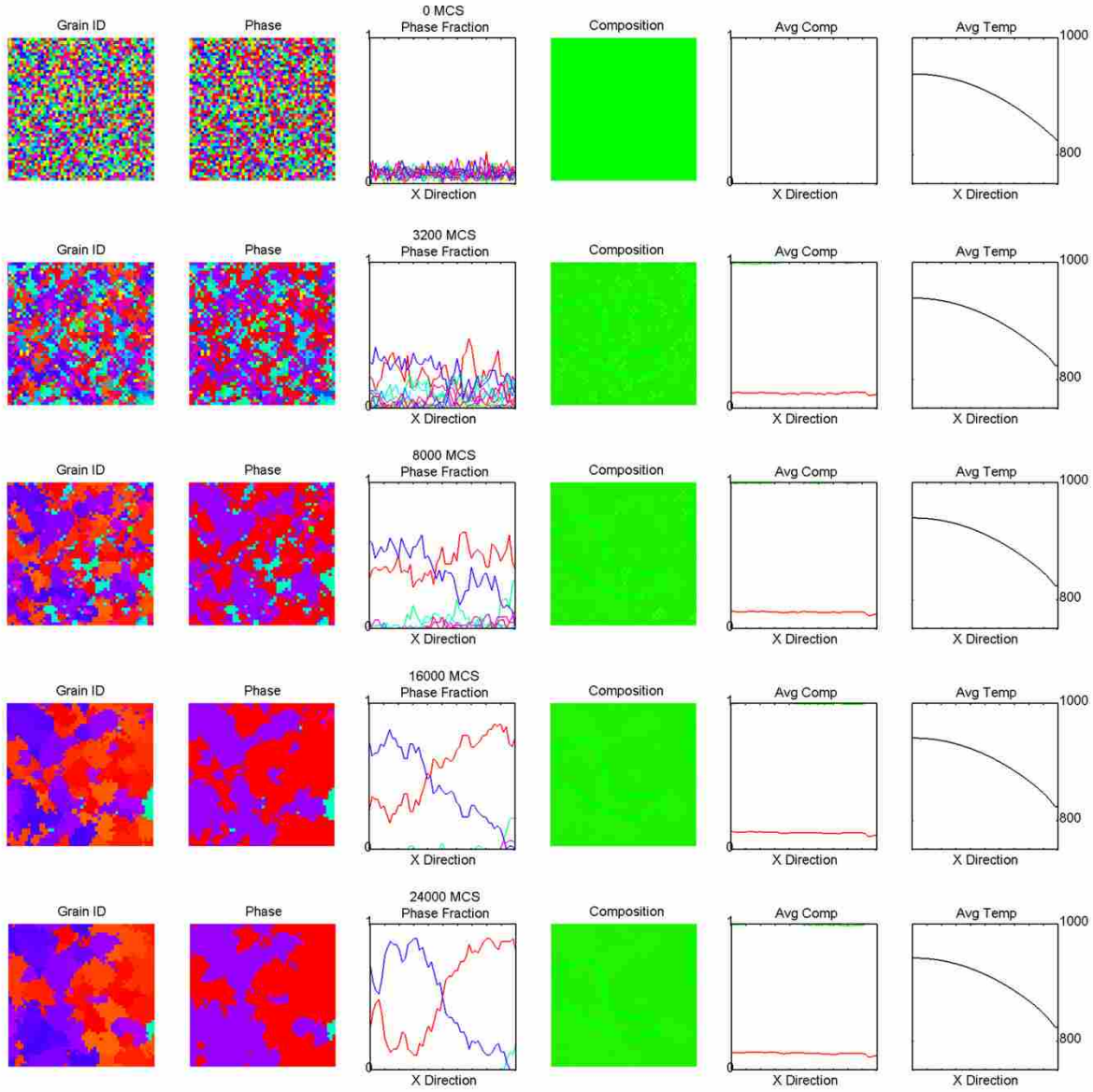

Figure A-7 Simulation 6 (Pu)

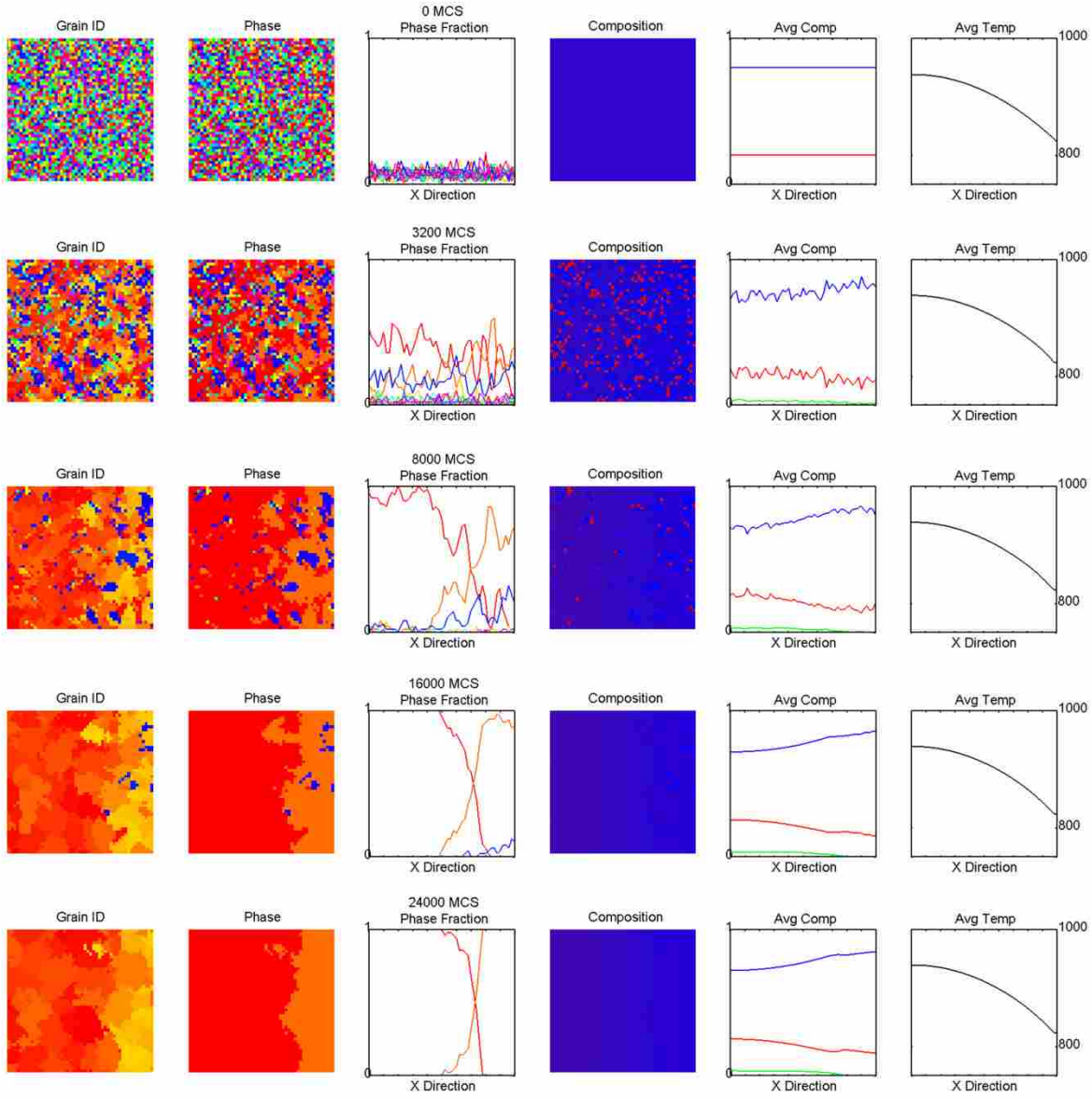

Figure A-8 Simulation 7 (U-80Zr)

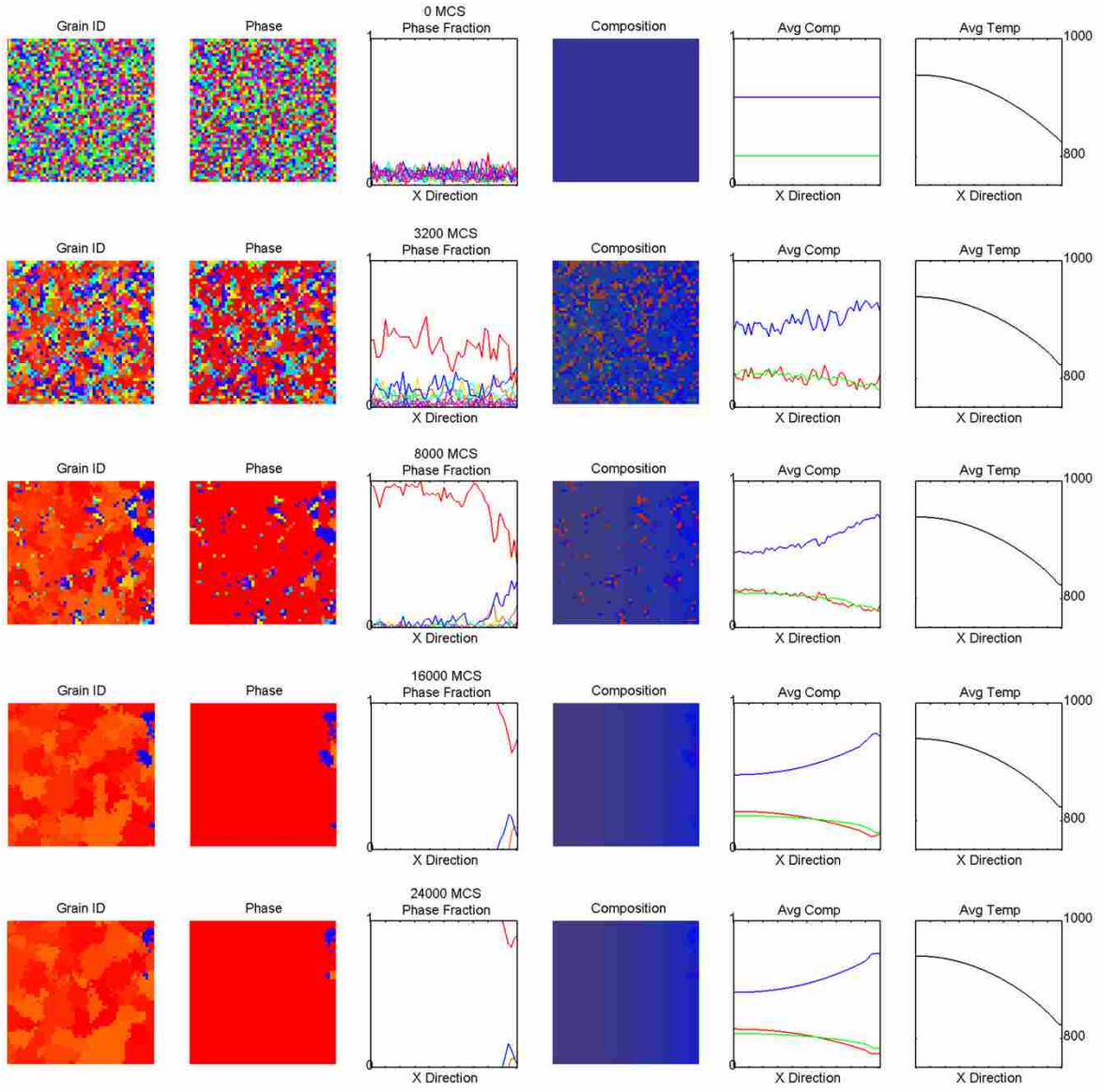

Figure A-9 Simulation 8 (U-20Pu-60Zr)

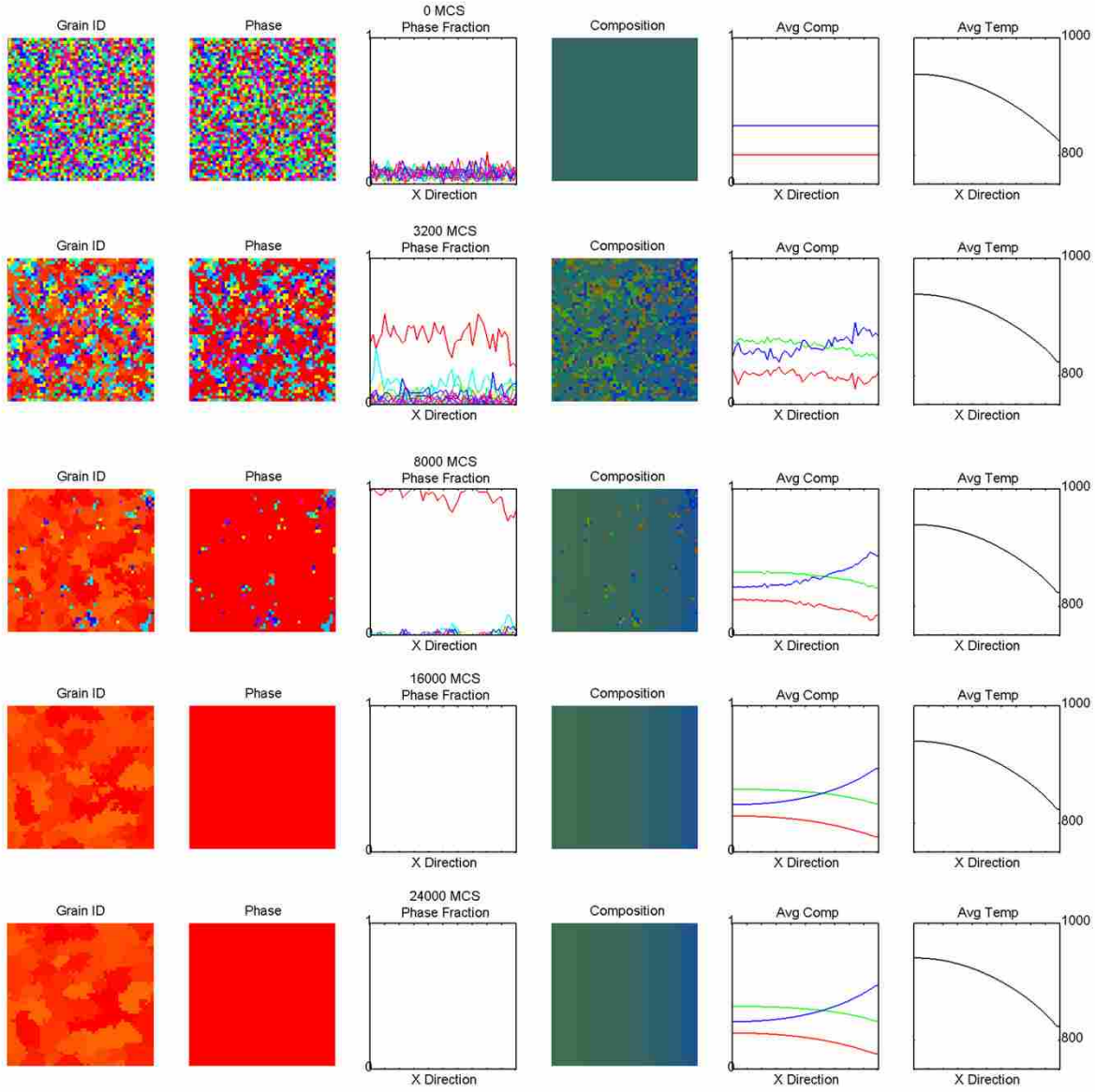

Figure A-10 Simulation 9 (U-40Pu-40Zr)

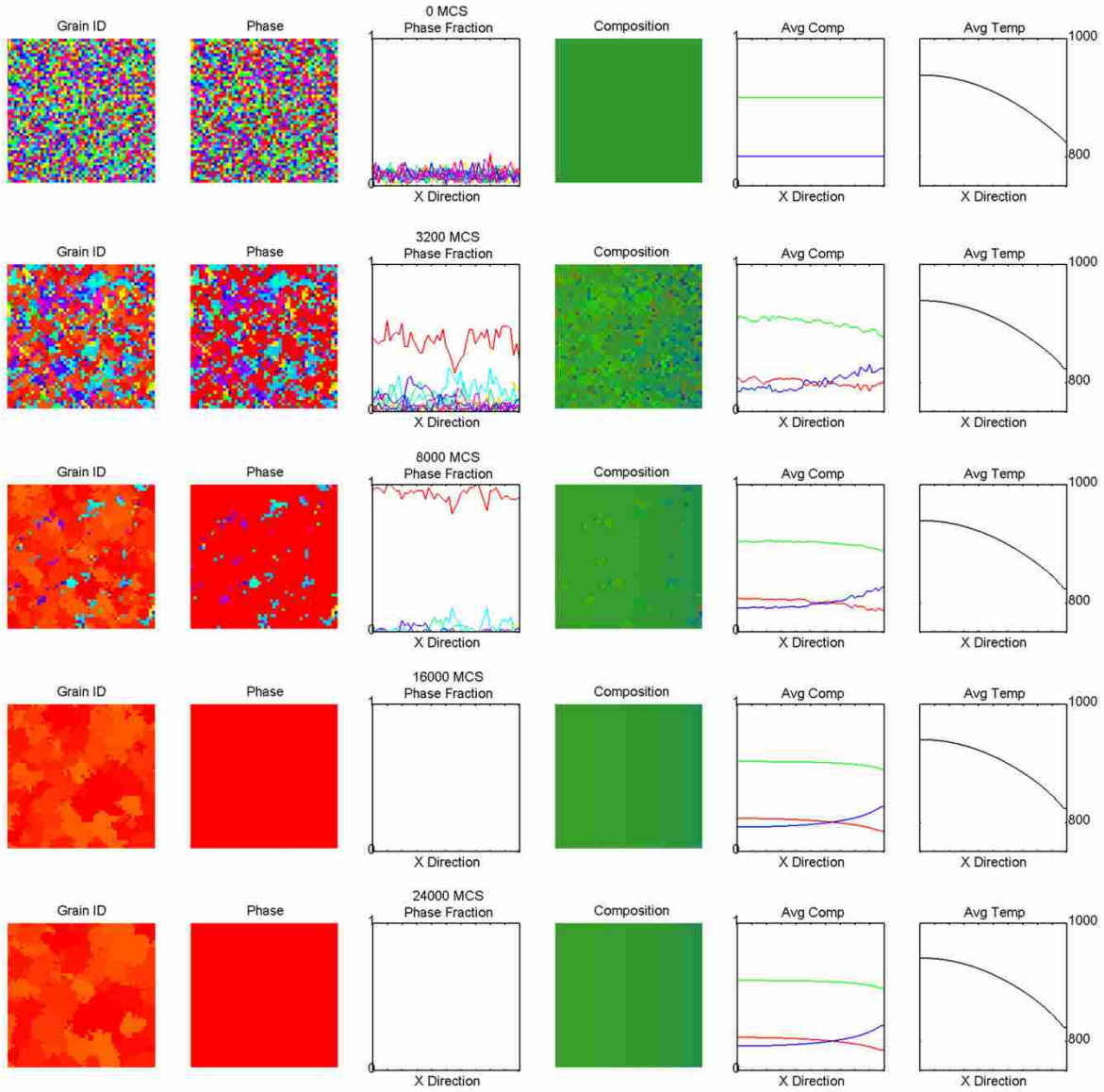

Figure A-11 Simulation 10 (U-60Pu-20Zr)

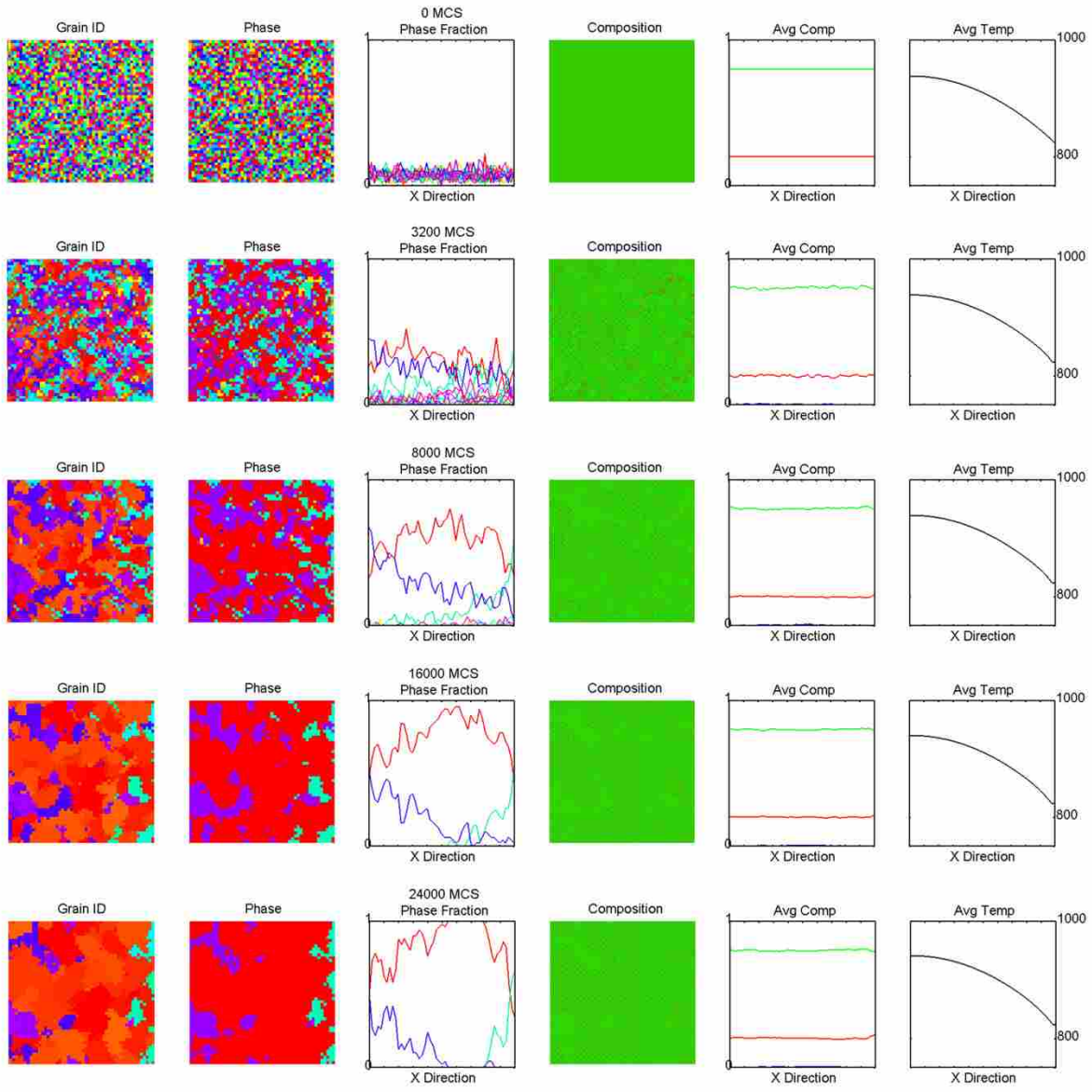

Figure A-12 Simulation 11 (U-80Pu)

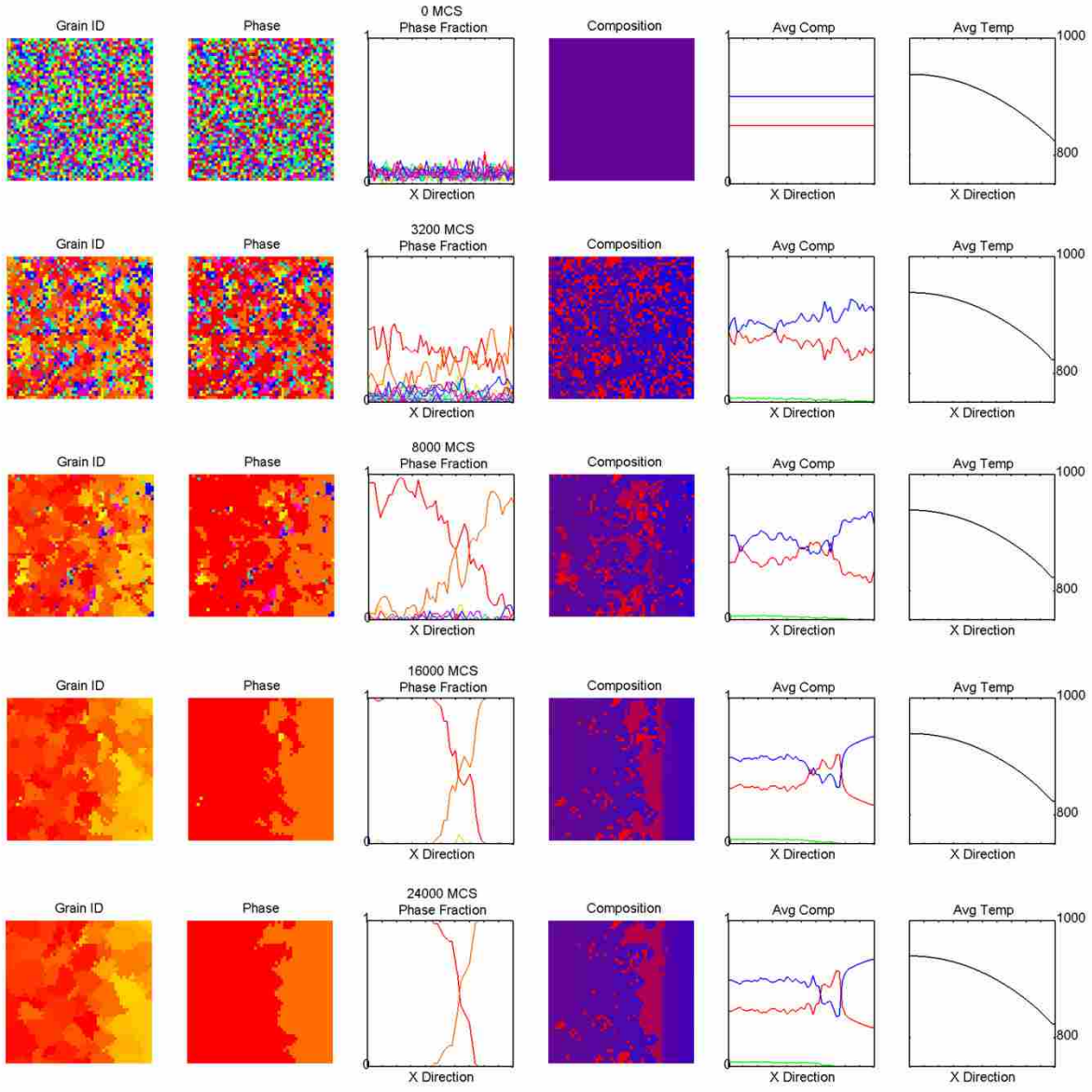

Figure A-13 Simulation 12 (U-60Zr)

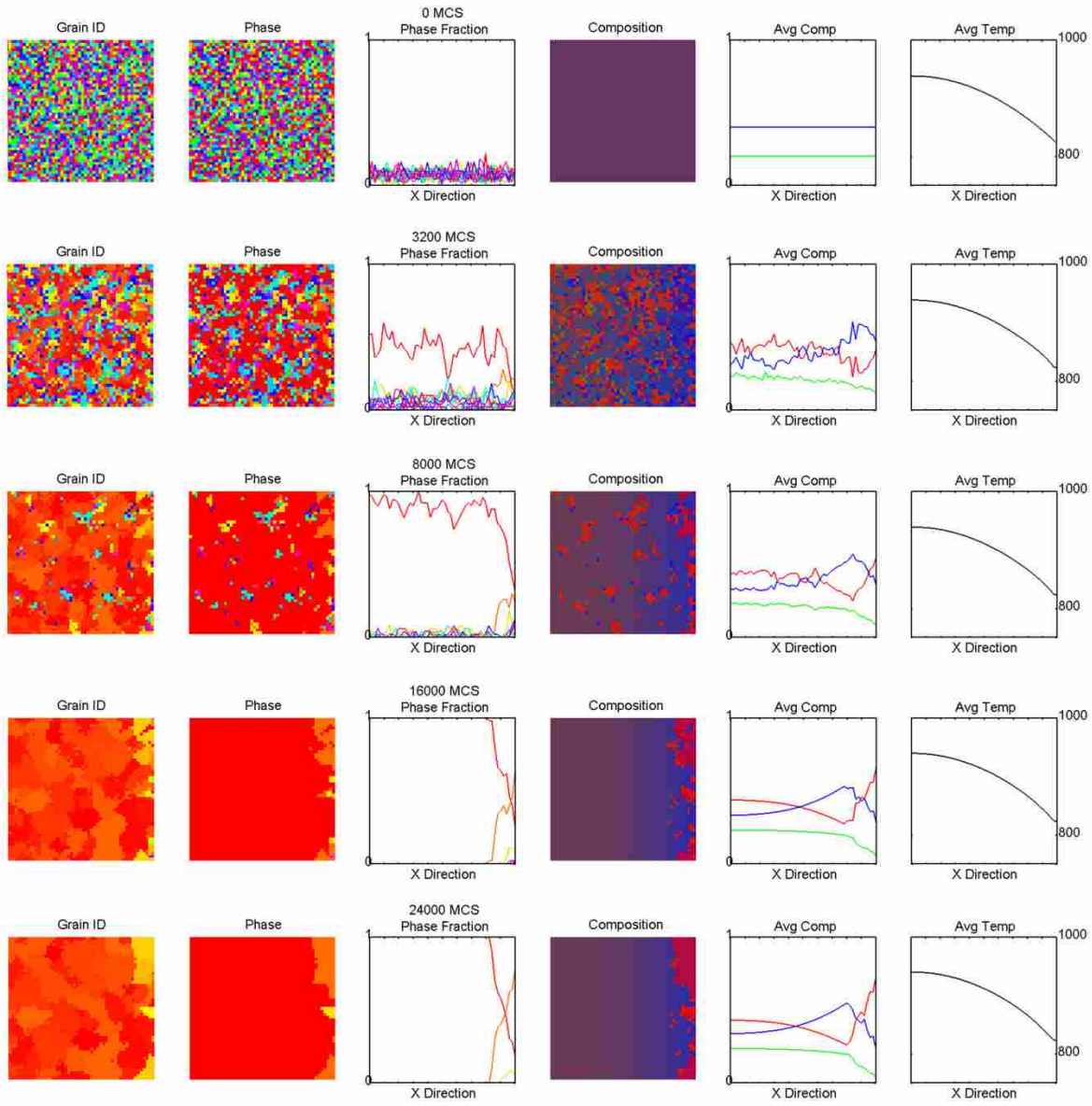

Figure A-14 Simulation 13 (U-20Pu-40Zr)

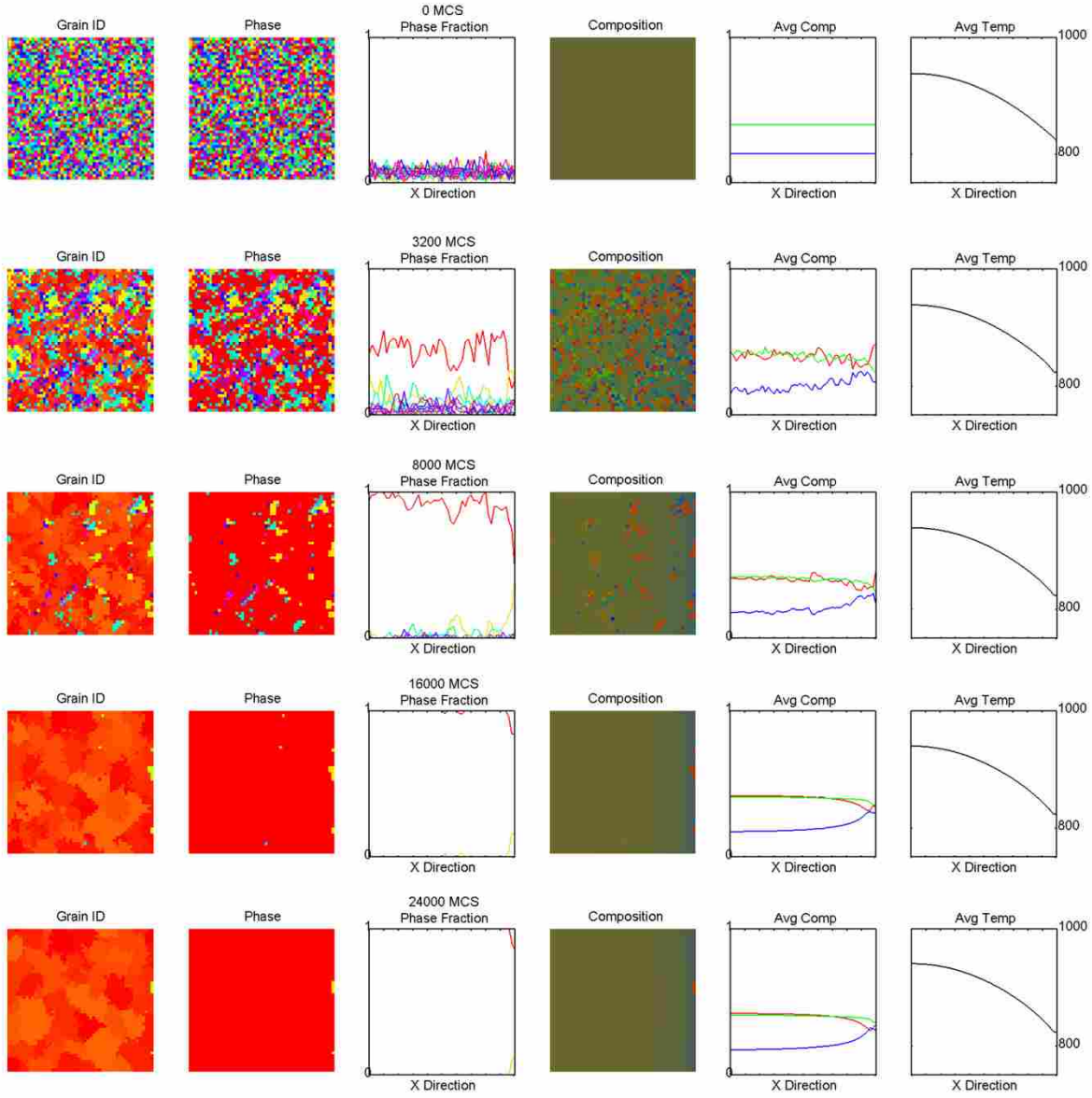

Figure A-15 Simulation 14 (U-40Pu-20Zr)

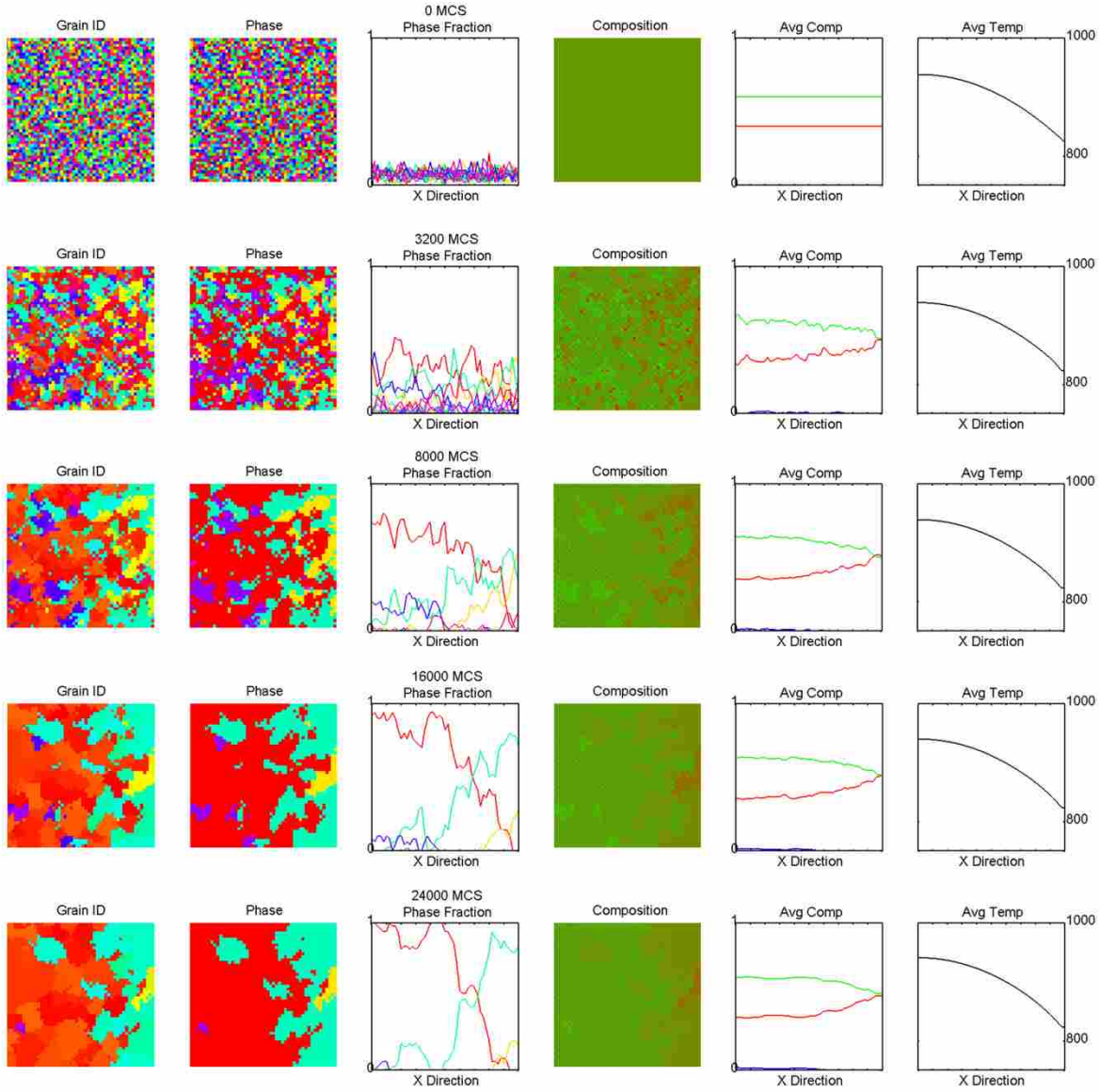

Figure A-16 Simulation 15 (U-60Pu)

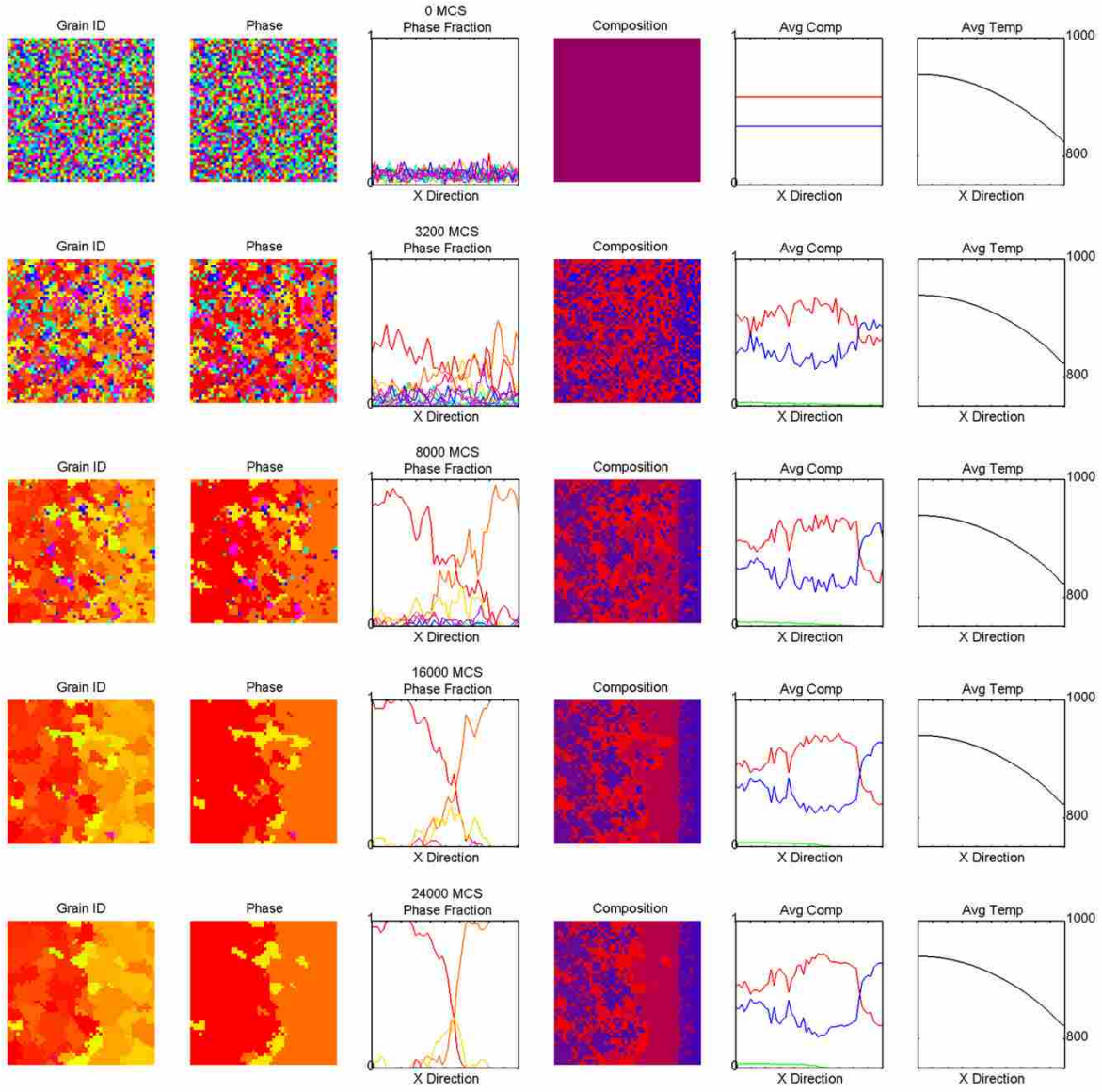

Figure A-17 Simulation 16 (U-40Zr)

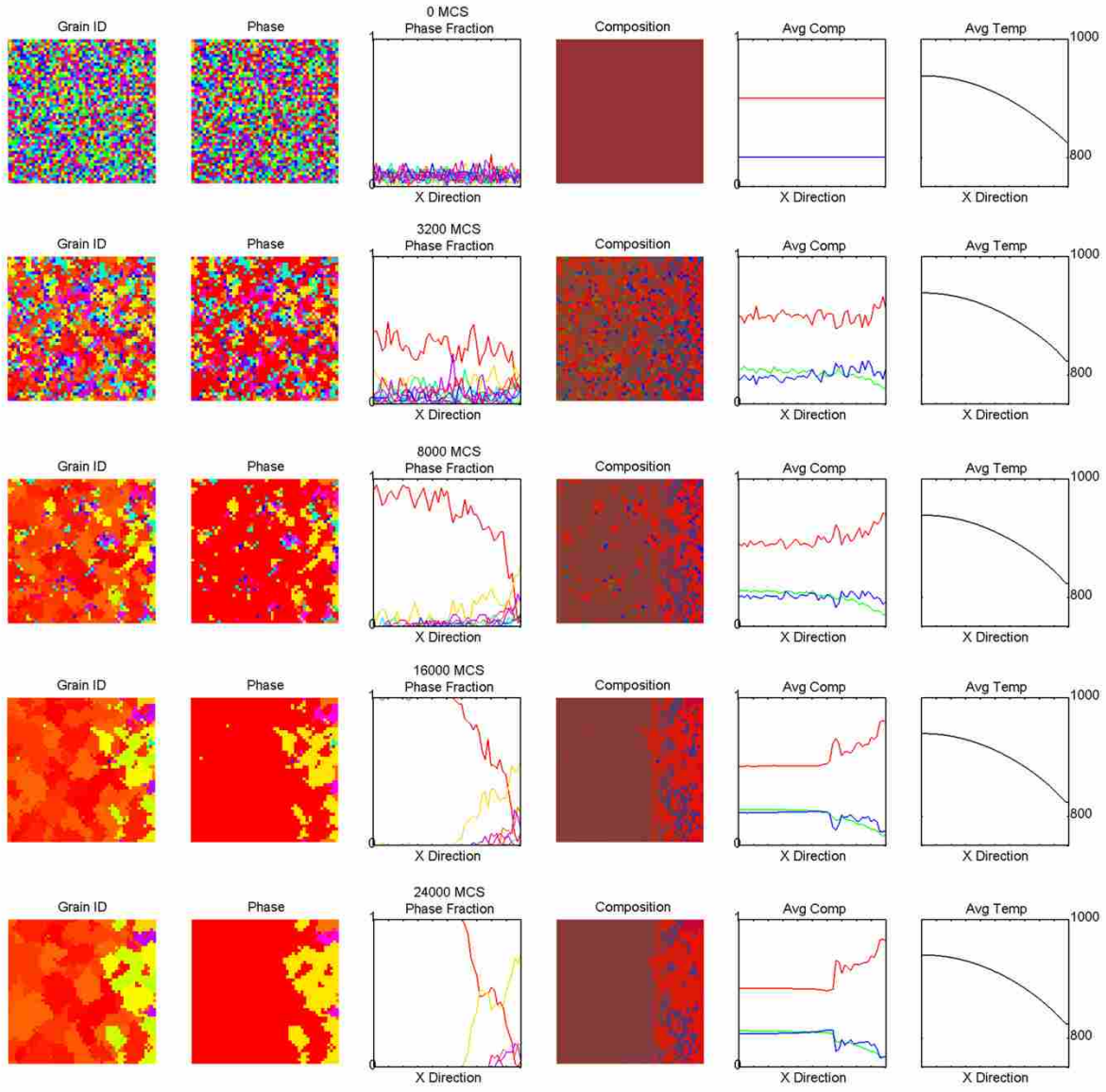

Figure A-18 Simulation 17 (U-20Pu-20Zr)

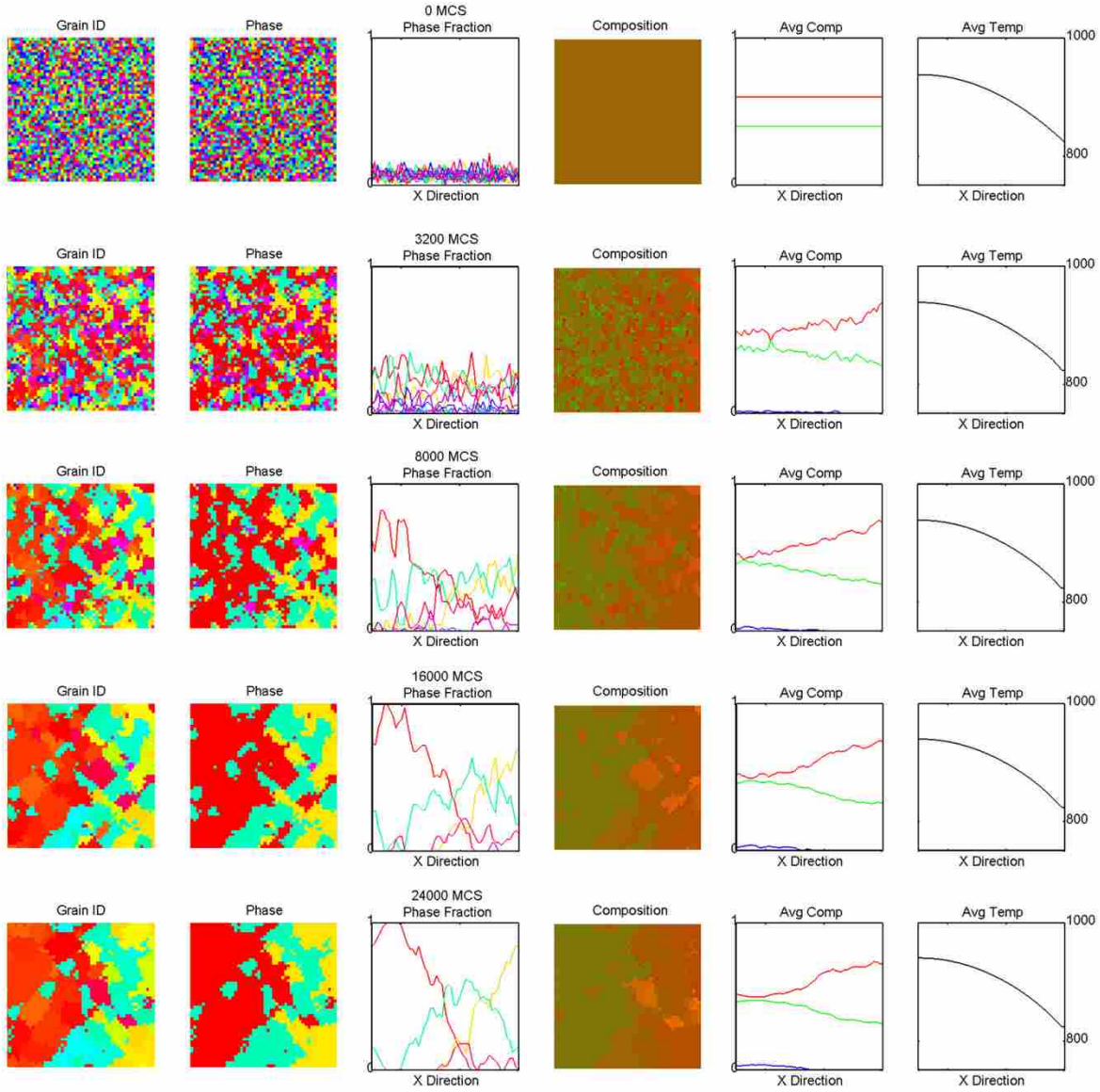

Figure A-19 Simulation 18 (U-40Pu)

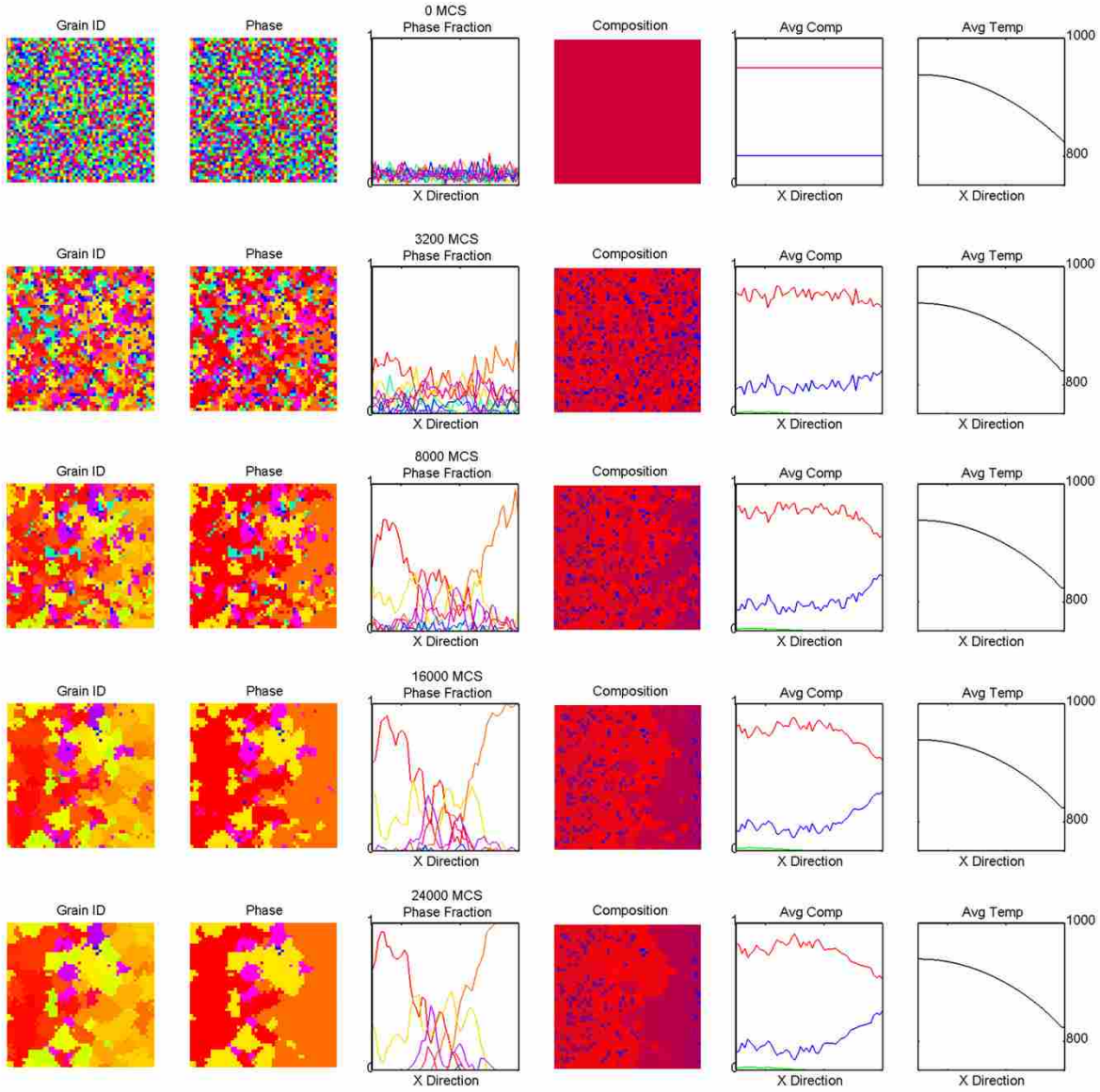

Figure A-20 Simulation 19 (U-20Zr)

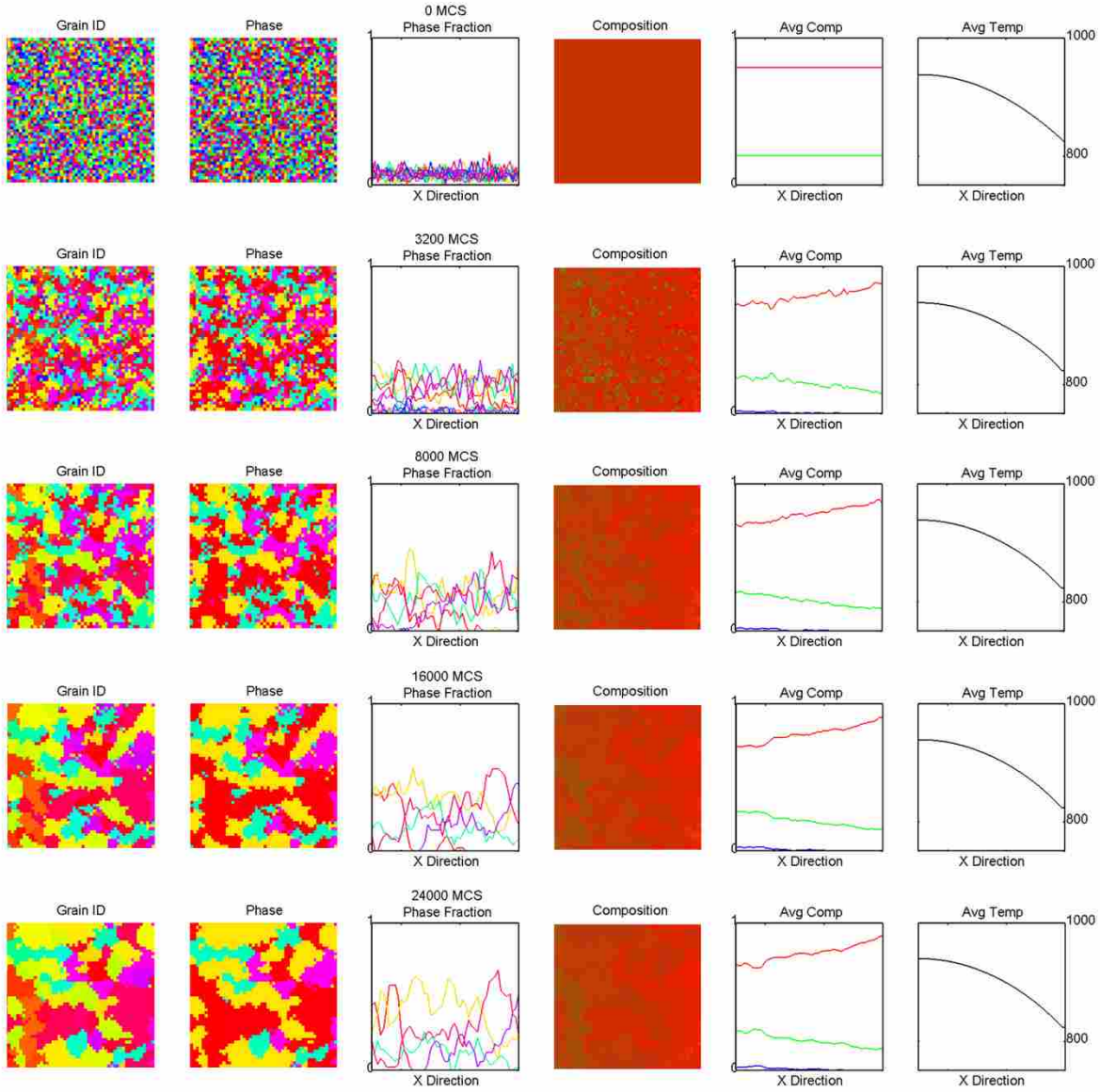

Figure A-21 Simulation 20 (U-20Pu)

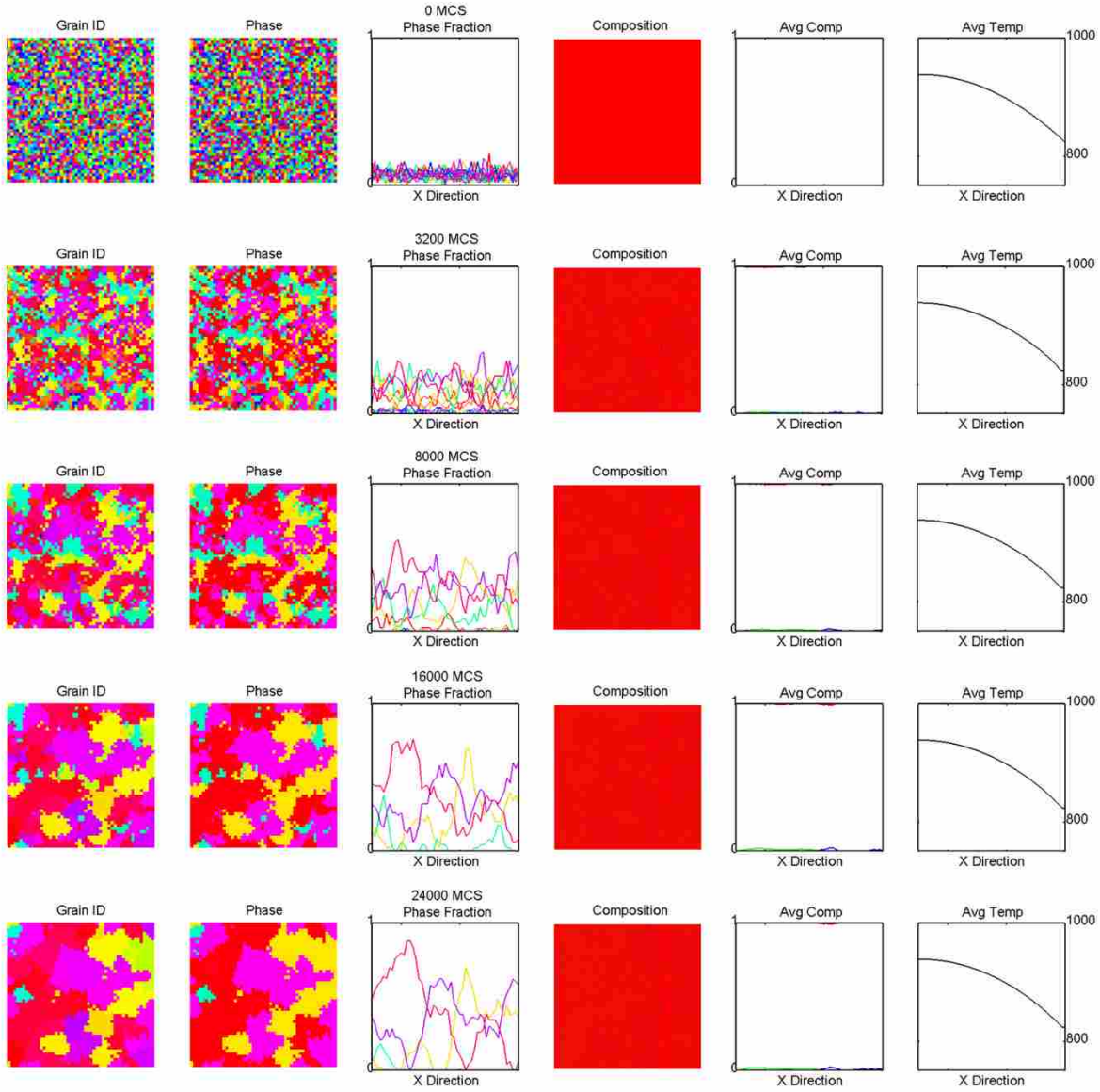

Figure A-22 Simulation 21 (U)